JGR Earth Surface

RESEARCH ARTICLE
10.1029/2019JF005506

The Application of Ensemble Wave Forcing to Quantify Uncertainty of Shoreline Change Predictions

Sean Vitousek[1,2], Laura Cagigal[3], Jennifer Montaño[3], Ana Rueda[4], Fernando Mendez[4], Giovanni Coco[3], and Patrick L. Barnard[1]

[1]Pacific Coastal and Marine Science Center, United States Geological Survey, Santa Cruz, CA, USA, [2]University of Illinois at Chicago, Chicago, IL, USA, [3]University of Auckland, Auckland, New Zealand, [4]University of Cantabria, Santander, Spain

Key Points:

- We assess uncertainty of ensemble Kalman filter data-assimilated shoreline change predictions using the spread of model trajectories
- We demonstrate an increase in modeled shoreline uncertainty due to ensemble wave conditions compared with single realization simulations
- Uncertainty in shoreline predictions can be quantified using a novel, straightforward relationship, derived analytically

Correspondence to:
S. Vitousek,
svitousek@usgs.gov

Citation:
Vitousek, S., Cagigal, L., Montaño, J., Rueda, A., Mendez, F., Coco, G., & Barnard, P. L. (2021). The application of ensemble wave forcing to quantify uncertainty of shoreline change predictions. *Journal of Geophysical Research: Earth Surface*, *126*, e2019JF005506. https://doi.org/10.1029/2019JF005506

Received 9 JAN 2020
Accepted 1 FEB 2021

Abstract Reliable predictions and accompanying uncertainty estimates of coastal evolution on decadal to centennial time scales are increasingly sought. So far, most coastal change projections rely on a single, deterministic realization of the unknown future wave climate, often derived from a global climate model. Yet, deterministic projections do not account for the stochastic nature of future wave conditions across a variety of temporal scales (e.g., daily, weekly, seasonally, and interannually). Here, we present an ensemble Kalman filter shoreline change model to predict coastal erosion and uncertainty due to waves at a variety of time scales. We compare shoreline change projections, simulated with and without ensemble wave forcing conditions by applying ensemble wave time series produced by a computationally efficient statistical downscaling method. We demonstrate a sizable (site-dependent) increase in model uncertainty compared with the unrealistic case of model projections based on a single, deterministic realization (e.g., a single time series) of the wave forcing. We support model-derived uncertainty estimates with a novel mathematical analysis of ensembles of idealized process models. Here, the developed ensemble modeling approach is applied to a well-monitored beach in Tairua, New Zealand. However, the model and uncertainty quantification techniques derived here are generally applicable to a variety of coastal settings around the world.

1. Introduction

Sandy shorelines respond to oceanographic and geologic processes at a variety of temporal (e.g., seconds to decades) and spatial (e.g., surf zone to ocean basin wide) scales. Thus, forecasting short- and long-term shoreline change remains difficult. Accurate predictions of shoreline movement in response to sea-level rise, changing wave climates, and reduced sediment supplies are increasingly sought to support coastal management, often out of fears that many beaches may be severely impacted by climate change (Le Cozannet et al., 2019; Masselink et al., 2016; Vitousek, Barnard, Limber, 2017).

Several well-tested and emerging models exist to represent shoreline change at a multitude of spatiotemporal scales (Roelvink 2011; Montaño et al., 2020; Ranasinghe 2020). Most shoreline models simplify complex coastal sediment transport processes to simulate the evolution of lines dividing beaches from adjacent water bodies, that is, "shorelines." Shoreline models are typically derived from a one-dimensional expression of conservation of sediment in the alongshore direction (Pelnard-Considere 1957). The evolution of shorelines is most often directly linked to oceanographic forcing from waves and sea level. In the most successful cases, the skill of shoreline models owes to strong connections between wave forcing and response (Robinet et al., 2016; Splinter et al., 2014). However, the growing uncertainty associated with future sea level and wave climate precludes a straightforward prediction along the forcing-response pathway. Hence, we are met with a pressing need for ensemble prediction, where once deterministic model predictions are replaced with probabilistic predictions (Davidson et al., 2017; Ranasinghe et al. 2012).

1.1. Ensemble Shoreline Change Modeling and Uncertainty

Probabilistic approaches to shoreline evolution are not entirely new (Vrijling & Meijer, 1992). Yet, the field of coastal change modeling remains dominated by single-realization, deterministic simulations with complex models at increasingly higher resolution (Roelvink & Walstra 2004). Several probabilistic approaches

are emerging, most of which rely on Monte Carlo methods, for example, running ensemble simulations of a deterministic model with random perturbations in parameters, different forcing conditions, etc., (Callaghan et al., 2013; Cowell et al., 2006; D'Anna et al., 2020; Davidson et al., 2017; Ding et al., 2018; Kroon et al., 2020; Le Cozannet et al., 2019; Reeve & Fleming 1997; Reeve et al., 2014; Ranasinghe et al. 2012; Ruggiero et al., 2007; Wang & Reeve, 2010; Zacharioudaki & Reeve, 2011). Among the multitude of coastal morphologic evolution models, we suggest that shoreline models may readily adopt ensemble methods for a variety of reasons, given below:

(1) Shoreline models are exceedingly affordable in computational cost compared with complex two-dimensional (2-D) and three-dimensional (3-D) physics-based sediment transport models (Antolínez et al., 2019; Reeve et al., 2016; Robinet et al., 2018; Vitousek et al. 2017). Hence, given an equivalent computational effort, the cheaper model facilitates the use of large ensembles in a Monte Carlo simulation (Davidson et al., 2017; Limber et al., 2018).
(2) Sediment transport models invariably rely on parameterizations of unresolved physics. Hence, unknown, tunable parameters abound for most sediment transport formulations. Ensemble modeling approaches facilitate the application of a wide range of potential parameter values to a given problem.
(3) Shoreline change is strongly driven by wave and sea-level forcing conditions, which, so far, cannot be predicted deterministically with any skill beyond time scales of a few days. Ensemble methods, on the other hand, might improve predictions of strongly forced, stochastic systems in a statistical sense.
(4) Shoreline movement is often 'noisy' due to hydrodynamic processes (e.g., tides, winds, waves, and wave runup), which vary on time scales of seconds to hours and manifest in observations collected sporadically over much longer time scales. Thus, the ensemble modeling approach allows the representation of noisy, unresolved processes in an otherwise deterministic model.
(5) Data assimilation can be readily applied to ensemble models (e.g., via ensemble Kalman filter methods) without incurring much computational overhead or extra analytical work (particularly, when compared with variational data-assimilation methods, see e.g., Bannister, 2017).
(6) The use of a multimodel ensemble (e.g., changing the underlying model formulation or governing equations across each ensemble member) is well suited to coastal change problems (Limber et al., 2018), since the 'best' performing model is often difficult to select a priori and it may change over space and time, due to future climatic uncertainty (Montaño et al., 2020).
(7) Uncertainty due to the aforementioned items and processes is treated in a straightforward manner (e.g., based on Monte Carlo) and, therefore, is easy to quantify based on the spread of model trajectories. For example, 95% confidence intervals can be easily determined by the band that encloses the middle 95% of model trajectories in the ensemble.

The current paper addresses the research question:

What are the differences in shoreline change projections and uncertainty estimates made with and without ensemble (i.e., probabilistic) wave conditions?

Uncertainty is often classified into two types, "epistemic," due to model errors, and "intrinsic," (or "aleatory") due to the inherent variability of stochastic processes like weather and waves (see e.g., Kroon et al., 2020; Murray et al., 2016; Roy & Oberkampf, 2011; Walker et al., 2003). The current paper seeks to quantify the intrinsic uncertainty of shoreline models due to waves. However, in doing so, we also attempt to understand and minimize epistemic (i.e., model) uncertainty using data assimilation. Davidson et al. (2010, 2017) were among the first to consider the intrinsic uncertainty of projected shoreline erosion due to wave climate variability. Davidson et al. (2017) used a Monte Carlo simulation of a shoreline model with ensemble wave conditions to produce erosion return-period curves, which provide probabilistic assessments of yet-to-occur extreme erosion events. In the current paper, we seek to address a similar research question to that of Davidson et al. (2017). However, here we also seek analytical means to quantify epistemic and intrinsic uncertainty, rather than via simulations alone. In the following sections, we demonstrate that by achieving a better (epistemic) understanding of the physics of shoreline change models, we can thus achieve a better understanding of the model's response and uncertainty due to the intrinsic variability of wave conditions.

1.2. Synopsis

The remainder of the paper is divided into four sections. Section 2 presents the methods used in the paper (i.e., the model governing equations and modifications of Yates et al. (2009), uncertainty quantification using ensembles of idealized models, the data-assimilation method, and the statistical-downscaling wave model to generate shoreline model input conditions). Section 3 presents Results of two distinct simulations of shoreline change (i.e., forced with and without ensemble wave forcing). Sections 4 and 5 present the Discussion and Conclusions, respectively. The paper also presents one appendix (Appendix A), which provides thorough mathematical analyses and derivations of the variance of ensembles of idealized process models, which are summarized in Section 2.2. The appendix supports the results of the model-derived uncertainty estimates presented in Section 3.

2. Methods

2.1. Shoreline Change Models

A variety of sediment transport processes (e.g., longshore transport, cross-shore transport, equilibrium profile adjustments due to sea-level rise, and sediment supply) contribute to coastal erosion, and a few "hybrid" coastal change models such as CoSMoS-COAST (Vitousek & Barnard, 2015; Vitousek et al. 2017), LX-Shore (Robinet et al., 2018), and COCOONED (Antolínez et al., 2019) are capable of resolving their combined effects. Previous works (Banno et al. (2015), Le Cozannet et al. (2019), Kroon et al. (2020), and D'Anna et al. (2020)) have investigated the modeling uncertainty associated with individual or combined sediment transport components. Here, we focus on addressing the uncertainty of cross-shore, wave-driven shoreline change, which is well simulated by equilibrium shoreline models (e.g., Davidson et al. 2013; Yates et al., 2009), and has been shown to capture up to 90% of the variance of the overall shoreline change in certain settings over short (i.e., annual to decadal) timescales (Vitousek et al. 2017). We begin with a careful consideration of the physics manifested in the popular Yates et al. (2009) equilibrium shoreline change model. We present a subtle modification of Yates et al. (2009), which improves our physical intuition of the behavior of the model and guides our analytical approach to quantify uncertainty, as discussed below.

2.1.1. Cross-Shore Equilibrium Shoreline Change Model (Yates et al., 2009)

The original Yates et al. (2009) equilibrium shoreline change model is given by

$$\frac{dY}{dt} = \underbrace{CE^{1/2}\Delta E}_{\text{cross-shore 'equlibirum' transport}} = CE^{1/2}\left(E - E_{\text{eq}}\right) = CE^{1/2}\left(E - aY - b\right) \tag{1}$$

where Y is the shoreline position, t is time, C is the erosion/accretion parameter (quasi-time-scale) parameter, $E = H_s^2$ is the wave energy (where H_s is the significant wave height), and $\Delta E = E - E_{\text{eq}}$ is the wave energy disequilibrium, where the equilibrium wave energy is a linear function of shoreline position given by $E_{\text{eq}} = aY + b$, where a and b are parameters representing the equilibrium slope (with dimensions of wave energy per length of shoreline change) and intercept (with dimensions of wave energy), respectively.

The role and dimensions of parameters C, a, and b in Equation 1 are not immediately obvious (see Table 1). Hence, subsequent works have modified the form of Equation 1 in order to improve clarity. Blossier et al. (2017a, 2017b) reformulated the Yates et al. (2009) model as

$$\frac{dY}{dt} = -\frac{1}{\tau}\left(Y - Y_{\text{eq}}\right) \tag{2}$$

where

$$Y_{\text{eq}} = \frac{E - b}{a} \tag{3}$$

and

Table 1
The Original (Yates et al., 2009) and Modified Equilibrium Shoreline Change Model Parameters, Roles, Dimensions, Units, Expected Sign, and Range of Values

Original parameter	Role	Dimensions	Commonly used units	Expected sign	Typical range of values[a]	Optimal values reported here (Tairua beach)
C	Erosion/accretion rate coefficient representing the magnitude/ time scale of erosion due to wave activity	length^{-2} time^{-1}	meters^{-2} days^{-1}, meters per meters^3 hr, wave energy^{-1} hr^{-1}	negative	−4 to 0	−0.19 meters^{-2} days^{-1}
a	The change in equilibrium wave energy per unit length of the shoreline	length, energy per length	meters, meters^2/meter	negative	−0.5 to −0.0001	−0.15 meters^2/meter
b	The background (e.g., mean) wave energy that characterizes the mean shoreline state	length^2, energy	meters^2, wave energy	positive	0 to 4	1.49 meters^2

Modified parameter	Role	Dimensions	Commonly used units	Expected sign	Typical range of values	Optimal values reported here (Tairua beach)
$\Delta T = \frac{1}{Cab^{1/2}}$	The equilibrium adjustment time scale	time	days, weeks	positive	1–4 weeks	28.6 days
$\Delta Y = \frac{b}{-a}$	The equilibrium shoreline excursion parameter	length	meters	positive	1 to 50	9.7 meters
$\hat{H}_s = \sqrt{b}$	The background (e.g., mean) wave height	length	meters	positive	0 to 2	1.22 meters

[a]Note some publications (e.g., Yates et al., 2009) calculate the wave energy as $E = \frac{1}{16}H_s^2$, whereas, for simplicity, we use $E = H_s^2$ throughout following Long and Plant (2012). Hence, the reported values of C, a, and b can vary as a result.

$$\tau = \frac{1}{CaE^{1/2}} \tag{4}$$

are the equilibrium shoreline position and the time scale for equilibrium adjustment, respectively. Equations 2 and 3 express the equilibrium state in terms (and dimensions) of shoreline position rather than in terms of wave energy like in Equation 1. Equation 2 is similar to the form of Miller and Dean (2004) and clarifies the equilibrium behavior and time scale. However, the dimensional role of parameters C, a, and b remain unintuitive. Previous studies have shown that parameters a and C are related (e.g., they both appear in the calculation of the time scale, τ) and can have compensating physical effects related to the beach dynamics (Castelle et al., 2014; Lemos et al., 2018). Thus, the model parameters are not always comparable between different sites. Here, we further modify the Yates et al. (2009) model based on Equation 2 so that the modified parameters (and their dimensions and signs) become easier to interpret physically. More specifically, we reformulate the original model parameters, so that the new parameters are all positive and have dimensions of simply length or time.

2.1.2. The Modified Yates et al. (2009) Model

We reformulate the Yates et al. (2009) model to improve the physical interpretation of the model parameters, while retaining *exactly the same* model dynamics. The modified Yates et al. (2009) model becomes:

$$\frac{dY}{dt} = \frac{1}{\tau}\left(Y_{\text{eq}} - Y\right) \tag{5}$$

where

$$Y_{\text{eq}} = \frac{E-b}{a} = \frac{b}{b}\frac{E-b}{a} = \frac{b}{a}\frac{E-b}{b} = -\left(-\frac{b}{a}\right)\frac{E-b}{b} = -\Delta Y\frac{H_s^2 - \hat{H}_s^2}{\hat{H}_s^2} \tag{6}$$

and

$$\tau = \frac{1}{CaE^{1/2}} = \frac{1}{CaE^{1/2}}\frac{b^{1/2}}{b^{1/2}} = \left(\frac{1}{Cab^{1/2}}\right)\frac{b^{1/2}}{E^{1/2}} = \left(\frac{1}{Ca\hat{H}_s}\right)\frac{\hat{H}_s}{H_s} = \Delta T\frac{\hat{H}_s}{H_s} = \Delta T\left(\frac{H_s}{\hat{H}_s}\right)^{-1} \quad (7)$$

This reformulation has replaced the three original model parameters (b, a, and C) with $\hat{H}_s$, ΔY, and ΔT, which represent combinations of the original parameters. The new model parameters are all positive and have intuitive dimensions of either length or time, as discussed below and in Table 1.

1. $\hat{H}_s = \sqrt{b} \approx \sqrt{\bar{E}}$ represents the background wave-height parameter in the equilibrium shoreline model. Here, $\hat{H}_s$ is simply a model parameter whose value is determined using data assimilation, however its magnitude typically bears a close resemblance to that of the average of the wave-height time series. Our initial estimates of $\hat{H}_s$ are based on the average of the wave-height time series, and the final, optimized value of $\hat{H}_s$ is generally close to the average wave height (e.g., within approximately ±50% of the average).
2. $\Delta Y = \frac{b}{-a}$ represents the characteristic cross-shore length scale of the shoreline erosion or accretion. Yates et al. (2019) identified $-b\,/\,a$ as the maximum beach width. However, here the ΔY parameter plays the role of an erosion/accretion excursion length-scale, as discussed below.
3. $\Delta T = \frac{1}{Cab^{1/2}}$ represents the time scale for equilibrium adjustment, as discussed below.

As discussed above, the reformulated parameters in Equations 5–7 represent an improvement over the parameters in Equation 1 from a dimensional viewpoint (see e.g., Table 1). However, it is important to note that the reformulation presented here has *not changed* any of the fundamental behavior of the original Yates et al. (2009) model (i.e., Equation 1 and Equations 5–7 are equivalent). The modification presented here has only reformulated the model by changing how we interpret its parameters.

Modifying the Yates et al. (2009) model (according to Equations 5–7) identifies two key variables that are critical to defining equilibrium-based shoreline change models: [1] the equilibrium shoreline position, Y_{eq}, in Equation 6 (which is driven by the wave conditions) and [2] the equilibrium time scale, τ, in Equation 7. Miller and Dean (2004) tested several different parameterizations for the equilibrium rate, $k = \tau^{-1}$, such as using a constant $k = k_\alpha$, $k \sim H_s^2$, $k \sim H_s^3$, $k \sim \Omega = \frac{H_s}{w_s T}$ (where Ω is the dimensionless fall velocity, w_s is the sediment fall velocity, and T is the wave period), although none emerged as the best alternative for their site of interest. Yates et al. (2009), on the other hand, considered the form $k = \tau^{-1} \sim H_s$ like in Equation 7. Many alternative parameterizations for the equilibrium position and time scale, such as those investigated by Miller and Dean (2004), might be easily integrated into the modified equilibrium model presented above by changing the time-varying wave factors $\frac{H_s^2 - \hat{H}_s^2}{\hat{H}_s^2}$ and $\left(\frac{H_s}{\hat{H}_s}\right)^{-1}$ in Equations 6 and 7, respectively. However, in the current paper, we only consider the behavior of the Yates et al. (2009) parameterizations of Y_{eq} and τ in Equations 6 and 7, respectively.

In Equation 6, the equilibrium shoreline position, Y_{eq}, is determined by the time-varying wave-energy anomaly term, $\frac{H_s^2 - \hat{H}_s^2}{\hat{H}_s^2}$, scaled by the shoreline excursion parameter ΔY. Note that the negative sign in Equation 6 scales positive wave-energy anomalies into erosion (i.e., $Y_{eq} < 0$), and vice versa, with negative wave-energy anomalies resulting in accretion. The role of the time-varying (inverse) normalized wave-height term $H_s\,/\,\hat{H}_s$ in Equation 7 is to decrease or increase the time scale for equilibrium adjustment, τ, during large or small wave events, respectively. During background wave conditions, $\tau = \Delta T$. In the current work, introducing a dedicated, constant background time-scale parameter, ΔT, is advantageous for several reasons:

1. Creating a new background time-scale parameter from the scalar triple product of the original Yates model parameters (i.e., $\Delta T = \frac{1}{Cab^{1/2}}$) makes parameter estimation (e.g., via optimization, data assimilation) more well-conditioned. As shown in the equation for ΔT above, changing any or all of parame-

ters C, a, or b in the data-assimilation step would alter the equilibrium time scale in the original Yates et al. (2009) formulation. Further, the original parameters C, a, and b generally have vastly different orders of magnitude, hence perturbations to the effective equilibrium time scale can become large when all of the original parameters (C, a, and b) are adjusted simultaneously during data assimilation. On the other hand, the modified parameters are assimilated more directly. For example, adjusting ΔT alone during the data-assimilation step directly changes the equilibrium time scale. A further advantage of the modified form is that all of the parameters have similar orders of magnitudes (e.g., $\Delta T \approx \mathcal{O}(1-10)$ days, $\Delta Y \approx \mathcal{O}(1-10)$ meters, and $\hat{H}_s \approx \mathcal{O}(1)$ meters), which reduces the need to introduce a normalization or feature scaling procedure in the parameter-estimation routine.

2. The original time scale $\tau = \frac{1}{CaE^{1/2}}$ of Blossier et al. (2017a, 2017b) (or equivalently the 'e-folding scale' of Yates et al. (2017)) varies with time. The newly introduced background time-scale parameter, ΔT within $\tau = \Delta T\left(H_s \,/\, \hat{H}_s\right)^{-1}$, is constant, yet it is easy to understand how time variability in the equilibrium time scale, τ, is introduced via the inverse of the normalized wave height term, $H_s \,/\, \hat{H}_s$. During large wave events (when erosion is usually expected), the time scale for equilibrium adjustment is decreased. Vice versa, the equilibrium time scale is increased during small wave events, which typically lead to accretion. This reformulation demotivates the practice (as in Yates et al. (2009)) of applying different erosion rate coefficients (i.e., C^+ and C^- for accretion and erosion, respectively), since it now becomes clear that such an accretion/erosion time-scale disparity is already partially captured using the time-varying normalized wave height factor in Equation 7. We note again that the reformulation presented here has not changed any of the underlying behavior of the original Yates et al. (2009) model, only our interpretation of it. If the additional C^+, C^- accretion/erosion time-scale disparity behavior is desired to be retained, then this can simply be accomplished by adopting $\Delta T^+ = \frac{1}{C^+ab^{1/2}}$ and $\Delta T^- = \frac{1}{C^-ab^{1/2}}$ parameters in the modified formulation, which is not pursued here.
3. During equilibrium (i.e., background) wave conditions, $\tau = \Delta T$. Hence, time scales of ΔT or greater will generally represent the beach recovery time scales for large erosion events followed by average or below average wave conditions, respectively. Further, the form of Equation 5 indicates that the total recovery time-scale ($\sim 3\Delta T$ to $4\Delta T$) during nominal wave conditions (i.e., when $Y_{\text{eq}} = 0$ since $H_s = \hat{H}_s$) is independent of the magnitude of erosion (i.e., Y_0), since during background wave conditions, the solution to Equation 5 is given by $Y \,/\, Y_0 = \exp\left(-t \,/\, \Delta T\right)$.

Finally, we make a remark on the 'equilibrium' nature of the shoreline dynamics manifested in models like Equations 5 and 6. As a thought experiment, assume that the shoreline could respond instantaneously to come into equilibrium with the wave conditions. Thus, the instantaneous shoreline position would be given by Equation 6 ($Y = Y_{\text{eq}}$), which predicts that when the wave energy is twice as large as the background value, $H_s^2 = 2\hat{H}_s^2$, then the shoreline position would be $Y = -\Delta Y$, that is one "unit" of the eroded shoreline excursion parameter. In practice, the assumption of instantaneous adjustment to equilibrium will grossly over-predict the shoreline erosion response to large wave events, due to the muting effect of the equilibrium adjustment time scale in Equation 5. For example, consider the data-assimilated ("best-fit") equilibrium shoreline change parameters at our study site, Tairua beach (described below): $\Delta Y \approx 10$, and $\hat{H}_s \approx 1.2$ m. The maximum observed relative wave-energy anomaly is $\max\left(\frac{H_s^2(t) - \hat{H}_s^2}{\hat{H}_s^2}\right) \approx 10$, yet the observed, maximally eroded shoreline position is −23 m, which is obviously far less than the $-10\Delta Y \approx -100$ m eroded position that would be predicted by Equation 6 under the assumption of instantaneous adjustment to equilibrium. Hence, the *time scale* for equilibrium adjustment plays an exceedingly important role in the dynamics of shoreline change.

The "best-fit" value of the time scale for equilibrium adjustment at Tairua beach, is given by $\Delta T = 28.6$ days during nominal wave conditions or $\tau = \Delta T\left(\frac{H_s}{\hat{H}_s}\right)^{-1} \approx 8$ days during the largest wave events (where $\max\left(H_s \,/\, \hat{H}_s\right) \approx 3.5$). This 8-day equilibrium adjustment time scale during large wave conditions seems to indicate that the beach erosion is "duration limited" (which borrows the term from the literature on

wind-generated waves). Here, we define "duration limited" to mean that the shoreline will likely not come to its equilibrium position during a single wave event, since large wave events typically peak and decline in far less than a week. Instead, the most eroded beach states (at Tairua and elsewhere) are likely to be produced by several wave events. Thus, we suggest it is important to recognize the sense of "dynamic equilibrium" that can only manifest in a differential equation, like Equation 5. Further, we suggest that although these models are called 'equilibrium shoreline models', truly reaching an 'equilibrium state' associated with large wave conditions (as described in Equation 6) may never occur. Instead, the beach perpetually exists in a transient state determined by the recent memory of large wave events that have forced the system out of its baseline state. We further explore the concepts of "dynamic equilibrium" and "beach memory" below.

2.1.3. Forcing, Damping, and "Beach Memory" in Equilibrium Shoreline Change Models

We prefer the modified equilibrium shoreline model presented in Equation 5 instead of that of Blossier et al. (2017a, 2017b) presented in Equation 2 (which is equivalent), because Equation 5 can be more easily interpreted as the combination of a wave forcing term and a damping term. For example,

$$\frac{dY}{dt} = \frac{1}{\tau}\left(Y_{\text{eq}} - Y\right) = \underbrace{f\left(t\right)}_{\text{wave forcing}} - \underbrace{\lambda_\tau Y}_{\text{damping}}. \tag{8}$$

In Equation 8, $f\left(t\right) = \frac{1}{\tau}Y_{\text{eq}} = -\frac{\Delta Y}{\Delta T}\frac{H_s}{\hat{H}_s}\frac{H_s^2 - \hat{H}_s^2}{\hat{H}_s^2}$ is the wave "forcing" term (based on the definitions of Y_{eq} and τ in Equations 6 and 7, respectively), which is purely a function of the model's wave input conditions (and the model parameters), and $-\lambda_\tau Y$ is the "damping" term, which is a function of the dependent variable Y and has a time-varying damping coefficient/rate of $\lambda_\tau = \tau^{-1} = \frac{1}{\Delta T}\frac{H_s}{\hat{H}_s}$. Classically, the appearance of the term $-\lambda_\tau Y$ in a first-order ordinary differential equation (i.e., with a left-hand side, $\frac{dY}{dt}$) represents (linear) damping or drag, where the λ_τ represents the damping or decay *rate* (see e.g., Moin 2010). The role of the damping term becomes more obvious when noting that the solution of $\frac{dY}{dt} = -\lambda_\tau Y$ is an exponential decay given by $Y = Y_0 \exp\left(-\lambda_\tau t\right)$. In Equation 8, the damping term acts to mute the effect of the forcing term, $f\left(t\right)$, with larger values of λ_τ causing larger amounts of damping. In the absence of damping, the system responds directly to forcing conditions.

In layman's terms, a shoreline model of the form presented in Equation 8 expresses the simple behavior that *beaches become increasingly harder to erode* (while in an eroded state). The treatment of wave forcing and damping is an extremely important aspect of the model/observations of Yates et al. (2009), which contrasts the underlying formulation of the equilibrium Shoreline Forecast (ShoreFor) model of Davidson et al. (2013).

The ShoreFor model as presented in Splinter et al. (2014) and Davidson et al. (2017) is given by

$$\frac{dY}{dt} = c^{\pm}P^{0.5}\frac{\Delta\Omega}{\sigma_{\Delta\Omega}} = c^{\pm}P^{0.5}\frac{\Omega_{\text{eq}}\left(t\right) - \Omega\left(t\right)}{\sigma_{\Delta\Omega}} \tag{9}$$

where $\Omega = \frac{H_s}{w_s T_p}$ is the dimensionless fall velocity (which, in this case, also represents the processes responsible for the equilibrium behavior), where w_s is the sediment fall velocity and T_p is the peak wave period, P is the wave power, $c^{\pm}$ are free calibration parameters representing erosion (−) and accretion (+), respectively. The equilibrium condition is $\Delta\Omega = \Omega_{\text{eq}}\left(t\right) - \Omega\left(t\right)$, and $\sigma_{\Delta\Omega}$ is the standard deviation of $\Delta\Omega$, which effectively normalizes the quantity in Equation 9. Ω_{eq} is the 'equilibrium' value of the dimensionless fall velocity, which is given by

$$\Omega_{\text{eq}}\left(t\right) = \frac{\sum_{j=1}^{2\phi}\Omega_j 10^{-j\Delta t/\phi}}{\sum_{j=1}^{2\phi}10^{-j\Delta t/\phi}} \tag{10}$$

following Wright et al. (1985), where Ω_j represents past values of the forcing conditions, where j is the number of days prior to the present time, Δt is the time step, and ϕ is the "memory decay" rate, which represents a damping time scale that is similar to τ.

Equation 10 is a weighted average of recent, antecedent forcing conditions. Thus, unlike in Yates et al. (2009), the entire right-hand side of Equation 9 is purely a function of the wave forcing conditions, that is,

$$\frac{dY}{dt} = \underbrace{f(t)}_{\text{wave forcing}}, \tag{11}$$

and is *not* a function of the shoreline position Y as in Equation 8 (See Example #5 in Appendix A for further details). In layman's terms, a shoreline model of the form presented in Equation 11 expresses the simple behavior that *beaches erode and accrete in response to recent wave forcing conditions* (and evolve independently of the current shoreline position). Although there is no explicit form of shoreline-position dependent "damping" in the ShoreFor model (i.e., Equations 9 and 10), the method places importance on recent wave conditions and provides mechanism for the shoreline position to equilibrate to persistent wave conditions, which acts somewhat similarly to damping.

The balance between forcing and damping is responsible for the equilibrium or baseline state of the shoreline (as well as the magnitude of possible departures from the equilibrium state). For example, the "steady state," time-averaged solution of the Yates et al. (2009) model (Equation 5) is $\langle Y \rangle = \langle Y_{\text{eq}} \rangle = -\Delta Y \frac{\langle H_s^2 \rangle - \hat{H}_s^2}{\hat{H}_s^2}$, which is approximately equal to zero provided $\langle H_s^2 \rangle \approx \hat{H}_s^2$, where $\langle\rangle = \frac{1}{T}\int_{t_0}^{t_0+T} () \, dt$ is an operator that represents the time average. In contrast, the tendency for ShoreFor simulations (Equation 11) to oscillate around a baseline state of $Y = 0$ over a long period of time is only achieved by near-perfect periodicity in the wave forcing conditions over time, that is, $\langle Y \rangle \approx 0$ if and only if $\langle f(t) \rangle \approx 0$. ShoreFor's lack of an explicit shoreline-position dependent damping term (e.g., $-\lambda_\tau Y$) allows for large shoreline fluctuations over time, which would otherwise be completely suppressed if damping were included. We demonstrate that the treatment of forcing and damping is also directly responsible for the concept of "beach memory."

We show in Appendix A (see Equation 52), that equilibrium models like Yates et al. (2009), which include a shoreline-dependent damping term as in Equation 8, have only a limited beach memory: they become uninfluenced by past shoreline states and storm-driven erosion events beyond a certain time scale. Mathematically, a lack of beach memory in the Yates et al. (2009) model means that the influence of past shoreline states decays exponentially with time, as demonstrated in Appendix A. On the other hand, equilibrium models like ShoreFor, which do not include a shoreline-dependent damping term as in Equation 11, have a near-perfect beach memory: the current shoreline position is uniquely determined by its initial condition and its entire time history of wave forcing conditions (see Equation 93 of Appendix A).

The differing treatments of forcing, damping, and beach memory, detailed above, represent fundamental and philosophical dissimilarities between Yates et al. (2009) and ShoreFor. Although the concept of damping is implicitly present in the name *equilibrium* shoreline model, the form and role of damping in the two different models was not immediately obvious and, until now, was never explicitly stated. In the following section, we demonstrate that the uncertainty of the shoreline model predictions is intimately related to the behaviors of forcing and damping manifested in their governing equations (cf., Equations 8 and 11). We demonstrate this via an analytical approach to assess the variance of ensembles of idealized process-based models that resemble Equation 8.

2.2. Uncertainty Quantification of Idealized Process Model Ensembles

In order to quantify uncertainty of ensemble shoreline-change simulations, we analyze idealized model ensembles that include the processes of forcing, damping, and noise, as given below

$$\frac{dY}{dt} = \underbrace{\frac{1}{\Delta T_f} f(t)}_{[1]\text{forcing}} - \underbrace{\lambda_\tau Y}_{[2]\text{damping}} + \underbrace{\underset{\sim}{\varepsilon}}_{[3]\text{noise}}. \tag{12}$$

Appendix A presents complete mathematical analyses and derivations of the uncertainty of idealized process models that include different combinations of the right-hand side terms in Equation 12. Here, we focus on and briefly summarize the uncertainty of the complete forced, damped, random walk ensemble of the form in Equation 12, due to its consistency with the Yates et al. (2009) equilibrium shoreline model described above in Equation 8. However, the complete set of idealized models investigated in Appendix A should apply to a wide range of ensemble modeling approaches throughout the geosciences.

The variance of a forced, damped, random walk ensemble (given by $\mathbf{Y}^{n+1} = \frac{\Delta t}{\Delta T_f}\mathbf{f}^n + \lambda \mathbf{Y}^n + \boldsymbol{\varepsilon}^n$, where $\lambda = 1 - \Delta t / \tau < 1$, Δt is the model time step, τ is a damping time scale, and ΔT_f is a forcing time scale as in Equation 75 of Appendix A) cannot grow indefinitely over time despite a continuous injection of noise because it is suppressed by damping (see Examples 2–4 in Appendix A). Instead, the variance becomes approximately constant in time and is given by

$$\sigma^2_{F,\max} = \underbrace{\left(\frac{\alpha}{\alpha - 1}\right)}_{\substack{\text{coefficient}\\ \text{related to}\\ \text{damping}}} \left[\underbrace{\underset{\sim}{\sigma^2}}_{\substack{\text{variance from}\\ \text{additive noise}\\ \text{(epistemic uncertainty)}}} + \underbrace{\left(\frac{\Delta t}{\Delta T_f}\right)^2 F \sigma_f^2}_{\substack{\text{variance from forcing}\\ \text{(intrinsic uncertainty)}}} \right] \tag{13}$$

which is derived in Equation 84 of Appendix A and is repeated here for clarity.

According to Equation 13, $\sigma^2_{F,\max}$ is set by the product of a coefficient related to damping, $\frac{\alpha}{\alpha - 1}$, which is generally larger than 1 (since $\alpha = \frac{1}{\lambda^2} > 1$ and $\lambda < 1$) and the sum of the individual variances contributed by the additive noise (where $\text{var}(\boldsymbol{\varepsilon}) \approx \sigma^2$, since $\boldsymbol{\varepsilon} \sim \mathcal{N}\left(0, \sigma^2\right)$ is a sample of normally distributed random, additive noise) and the forcing (where $\text{var}\left(\mathbf{f}\right) \approx \sigma_f^2$). Focusing first on the effect of damping, we see, intuitively, that increasing the amount of damping decreases the maximum variance $\sigma^2_{F,\max}$ and vice versa. Focusing next on the effect of forcing, we see the presence of a factor F in the variance contributed by the forcing in Equation 13. This factor acts to increase the variance contributed by a general forcing function relative to that of a random forcing function (compare Examples 3 and 4 in Appendix A). Factor F in Equation 13 is given by

$$F \approx 1 + \frac{\sum_{i \neq j} \text{cov}\left(\mathbf{f}^i, \mathbf{f}^j\right)}{\sum_{i=1}^{N} \text{var}\left(\mathbf{f}^i\right)}, \tag{14}$$

which is derived in Equations 82 and 83 of Appendix A and is repeated here for clarity. In the current application, we find that the covariance of the forcing ensemble increases the overall variance of the forcing term in Equation 13 by a factor of $F \approx 15$ compared to the case of random forcing conditions. Qualitatively, this increase makes sense: when the forcing conditions (e.g., waves) are auto-correlated, they will generally cause persistent changes (e.g., erosion or accretion) over time compared to random forcing conditions that frequently change sign. Thus, the cumulative effect of the forcing on the model's state (and its variance) is increased.

In the context of shoreline change simulations, the first and second variance terms within the square brackets of Equation 13 represent the epistemic and intrinsic uncertainty, respectively. The first term (i.e., the variance from the additive noise) represents (a portion of the overall) epistemic uncertainty because it is a user-prescribed parameter that specifies the accuracy limitations of the model due to unresolved processes. The second term (the variance from the forcing) represents the intrinsic uncertainty because it inherently results from the variability of the forcing conditions (e.g., waves). Further, Equation 13 indicates that a uniformly-forced model (with $\mathrm{var}\left(\mathbf{f}\right) = \sigma_f^2 = 0$) contributes no variance with respect to the forcing term (since the uniform forcing is applied consistently to *all* ensemble members). Hence, all of the intrinsic uncertainty is missing from uniformly forced simulations, and the variance of a uniformly forced ensemble is given by

$$\sigma_{\max}^2 = \left(\frac{\alpha}{\alpha - 1}\right)\sigma^2 \tag{15}$$

We further explore the behaviors of epistemic and intrinsic uncertainty in the simulations presented below in Results.

2.3. Data-Assimilation Method

Here, we utilize an ensemble Kalman filter (EnKF) data-assimilation method following Evensen (1994). The ensemble Kalman filter method has not been utilized in the context of shoreline modeling, until now. However, the method has been used in the nearshore processes literature for parameter estimation and bathymetric inversion (see e.g., Wilson et al., 2010, 2014).

Based on available observations, the EnKF data-assimilation method computes a Bayesian update of an ensemble of the model state, $\boldsymbol{\psi} = \left[\vec{\psi}_1 \quad \vec{\psi}_2 \quad \cdots \quad \vec{\psi}_{N_{\mathrm{ens}}}\right]$, where each state vector $\vec{\psi}$ of the N_{ens} member ensemble contains the combination of the model solution and parameters (see e.g., Equation 27 below). The EnKF method automatically adjusts the model state during the simulation to best fit any available shoreline observations at the concurrent time step, via an optimal interpolation that accounts for the uncertainty of both the model and observations. The procedure of the data-assimilation method is given by:

1. Run the forward model with added noise:

$$\boldsymbol{\psi}^* = \mathbf{F}\left(\boldsymbol{\psi}^{\mathbf{n}}\right) + \boldsymbol{\varepsilon} \tag{16}$$

   where $\boldsymbol{\psi}^*$ is the forecasted state vector (see e.g., Equation 27 below), $\boldsymbol{\psi}^n$ is the model state vector at time step n, $\mathbf{F}$ is the operation of the (forward) model advancement for a single time step (see e.g., Equation 26 below) and $\boldsymbol{\varepsilon} \sim \mathcal{N}\left(0, \sigma^2\right)$ is a sample of random, additive noise drawn from a normal distribution with zero mean and user-prescribed variance σ^2.
   In the absence of data to assimilate, the inverse model (i.e., the data-assimilation method computed via steps 2–4 below) is not computed, and the model state vector at time step $n + 1$ is simply predicted by the (forward) model, i.e., $\boldsymbol{\psi}^{n+1} = \boldsymbol{\psi}^*$.
2. Calculate the covariance of the model ensemble for $\boldsymbol{\psi}^*$:

$$\mathbf{P} = \mathrm{cov}\left(\boldsymbol{\psi}^*\right) = \frac{1}{\mathrm{N_{ens}} - 1}\sum_{i=1}^{\mathrm{N_{ens}}}\left(\psi_i^* - \bar{\psi}^*\right)\left(\psi_i^* - \bar{\psi}^*\right)^T \tag{17}$$

   where $\bar{\psi}^*$ is the ensemble average state vector $\boldsymbol{\psi}^*$. Compared with the extended Kalman filter (EKF) approach (used in Long & Plant, 2012; Vitousek et al. 2017), Equation 17 replaces the analytical derivation and advancement of the error covariance matrix $\mathbf{P}$, which is calculated from the Jacobian matrix (i.e., the matrix of partial derivatives) of the forward model $\mathbf{F}$. Hence, the EnKF method using Equation 17 requires very little computational overhead and no analytical work to derive the Jacobian matrix, in contrast to the EKF method. On the other hand, the EnKF necessarily requires running an ensemble, whereas the EKF method can be run on a single model realization.

3. Calculate the so-called Kalman gain, $\mathbf{K}$, according to the Equation

$$\mathbf{K} = \mathbf{P}\mathbf{H}^T\left(\mathbf{H}\mathbf{P}\mathbf{H}^T + \mathbf{R}\right)^{-1}, \tag{18}$$

where $\mathbf{H}$ is the operator relating the model and observations (see e.g., Equation 28) and $\mathbf{R} = \frac{1}{N_{\text{ens}} - 1}\sum_{i=1}^{N_{\text{ens}}}\left(\varepsilon_{\text{obs}}\right)_i\left(\varepsilon_{\text{obs}}\right)_i^T$ is the covariance matrix of the perturbed observations, where $\varepsilon_{\text{obs}} \sim \mathcal{N}\left(0, \sigma_{\text{obs}}^2\right)$ is the noise associated with the observations, which we assume to be drawn from a normal distribution with zero mean and variance σ_{obs}^2.

4. Update the state vector:

$$\boldsymbol{\psi}^{n+1} = \boldsymbol{\psi}^* + \mathbf{K}\left(\underbrace{\left[\boldsymbol{\psi}_{\text{obs}}^{n+1} + \boldsymbol{\varepsilon}_{\text{obs}}\right]}_{\text{perturbed observations}} - \underbrace{\mathbf{H}\boldsymbol{\psi}^*}_{\text{model prediction for the observed locations/varaibales}}\right) \tag{19}$$

where $\boldsymbol{\psi}^{n+1}$ is final (analysis) state vector. Equation 19 demonstrates that the Kalman gain $\mathbf{K}$ effectively scales/translates the mismatch between the observations and the model into adjustments made to the state vector $\boldsymbol{\psi}$. Note that the bracketed term in Equation 19 represents perturbation of the observed state vector, $\boldsymbol{\psi}_{\text{obs}}^{n+1}$, with the representative observation noise, $\boldsymbol{\varepsilon}_{\text{obs}}$.

Finally, we present a modification of the model equations to preserve the expected signs of the model parameters during the data-assimilation step following the approach in Vitousek et al. (2017). As mentioned previously, several of the model parameters (e.g., ΔT, ΔY, and $\hat{H}_s$) are positive. However, there is no guarantee that the data-assimilation method (specifically, in Equation 19) will preserve the expected signs of the parameters. Hence, we modify the model equations following Vitousek et al. (2017) to ensure that the parameters retain their expected sign during the data-assimilation procedure.

The numerical method for Equation 5 is given by

$$\frac{Y^{n+1} - Y^n}{\Delta t} = \frac{1}{\Delta T}\left(\frac{H_s^n}{\hat{H}_s}\right)\left(Y_{\text{eq}}^n - Y^n\right) = \underbrace{-\frac{\Delta Y}{\Delta T}\left(\frac{H_s^n}{\hat{H}_s}\right)\frac{\left(H_s^n\right)^2 - \left(\hat{H}_s\right)^2}{\left(\hat{H}_s\right)^2}}_{\text{wave forcing}} \underbrace{- \frac{1}{\Delta T}\left(\frac{H_s^n}{\hat{H}_s}\right)Y^n}_{\text{damping}} \tag{20}$$

where

$$Y_{\text{eq}}^n = -\Delta Y\frac{\left(H_s^n\right)^2 - \left(\hat{H}_s\right)^2}{\left(\hat{H}_s\right)^2} \tag{21}$$

and where the first-order accurate forward Euler time stepping method (see e.g., Moin 2010) has been used. Equation 20 can be rearranged as an update equation for Y given by

$$Y^{n+1} = Y^n + \frac{\Delta t}{\Delta T}\left(\frac{H_s^n}{\hat{H}_s}\right)\left(Y_{\text{eq}}^n - Y^n\right) = Y^n \underbrace{-\Delta t\frac{\Delta Y}{\Delta T}\left(\frac{H_s^n}{\hat{H}_s}\right)\frac{\left(H_s^n\right)^2 - \left(\hat{H}_s\right)^2}{\left(\hat{H}_s\right)^2}}_{\text{wave forcing}} \underbrace{- \frac{\Delta t}{\Delta T}\left(\frac{H_s^n}{\hat{H}_s}\right)Y^n}_{\text{damping}}. \tag{22}$$

We modify the parameters in Equation 22 according to

$$\Delta T = \Delta T_0 \exp\left(\sigma_1 \Delta T_1\right) \tag{23}$$

$$\Delta Y = \Delta Y_0 \exp\left(\sigma_1 \Delta Y_1\right) \tag{24}$$

$$\hat{H}_s = \left(\hat{H}_s\right)_0 \exp\left(\sigma_1 \left(\hat{H}_s\right)_1\right) \tag{25}$$

where ΔT_0, ΔY_0, and $\left(\hat{H}_s\right)_0$ are the initial parameter estimates and the static parameter σ_1, which is set to a value of 0.5 as in Vitousek et al., 2017, influences the range of the possible values of the assimilated parameters. Note that in Equations 23–25, ΔT_1, ΔY_1, and $\left(\hat{H}_s\right)_1$ can be positive or negative but the resulting values for ΔT, ΔY, and $\hat{H}_s$ will be positive.

After substituting Equations 23–25 into Equation 22, the model equation becomes

$$Y^{n+1} = Y^n + \frac{\Delta t}{\Delta T_0 \exp(\sigma_1 \Delta T_1)} \left(\frac{H_s^n}{(\hat{H}_s)_0 \exp(\sigma_1 (\hat{H}_s)_1)} \right) \left(-\Delta Y_0 \exp(\sigma_1 \Delta Y_1) \frac{(H_s^n)^2 - ((\hat{H}_s)_0 \exp(\sigma_1 (\hat{H}_s)_1))^2}{((\hat{H}_s)_0 \exp(\sigma_1 (\hat{H}_s)_1))^2} - Y^n \right) \tag{26}$$

which represents the forward model, **F**, in Equation 16. The state vector used in data assimilation is thus given by

$$\vec{\psi} = \left[Y \quad \Delta T_1 \quad \Delta Y_1 \quad \left(\hat{H}_s\right)_1 \right]^T, \tag{27}$$

and hence the operator relating the model to the observations is given by

$$\boldsymbol{H} = \left[1 \quad 0 \quad 0 \quad 0 \right]^T. \tag{28}$$

Here, Equation 28 simply indicates that observations exist only for the shoreline position Y in the state vector $\vec{\psi}$ given by Equation 27, and likewise that we have no direct observations of the values of the model parameters ΔT_1, ΔY_1, and $\left(\hat{H}_s\right)_1$.

In summary, the change of variables from Equations 22–26 allows the data-assimilation method to adjust the parameters ΔT_1, ΔY_1, and $\left(\hat{H}_s\right)_1$ (which can be positive or negative) and the original parameters ΔT, ΔY, and $\hat{H}_s$ will retain their requisite sign.

2.4. Calibration/Validation of the Multivariate, Stochastic Climate-Based, Wave Emulator to Generate Ensemble Wave Conditions at Tairua Beach, New Zealand

Wave modeling remains a critical component to assess coastal change (Antolínez et al., 2016; Camus et al., 2017; Hegermiller et al., 2016; Robinet et al., 2016). Here, we briefly describe the wave modeling approach, based on the Multivariate, Stochastic Climate-Based, Wave Emulator of Cagigal et al. (2020), used to generate ensemble wave forcing conditions at our current study site, Tairua beach, New Zealand. The complete methodology of the Wave Emulator is presented in Cagigal et al. (2020). However, we briefly summarize the methodology of the model at Tairua beach in Figure 1. The wave model reproduces not only the historical intraseasonal, seasonal, and interannual variability, but also the intrastorm chronology, which is a key issue for shoreline change models as the time-history and duration of storms can cause very different erosion or accretion patterns. The wave chronology is also important in the quantification of uncertainty evidenced by the role of the auto-correlation factor, F, in Equation 84 of Appendix A.

The validation of the wave parameters with hindcasted wave conditions at Tairua beach, NZ is shown in Figure 2. The occurrence probabilities of the different wave parameters in the bivariate space are explored

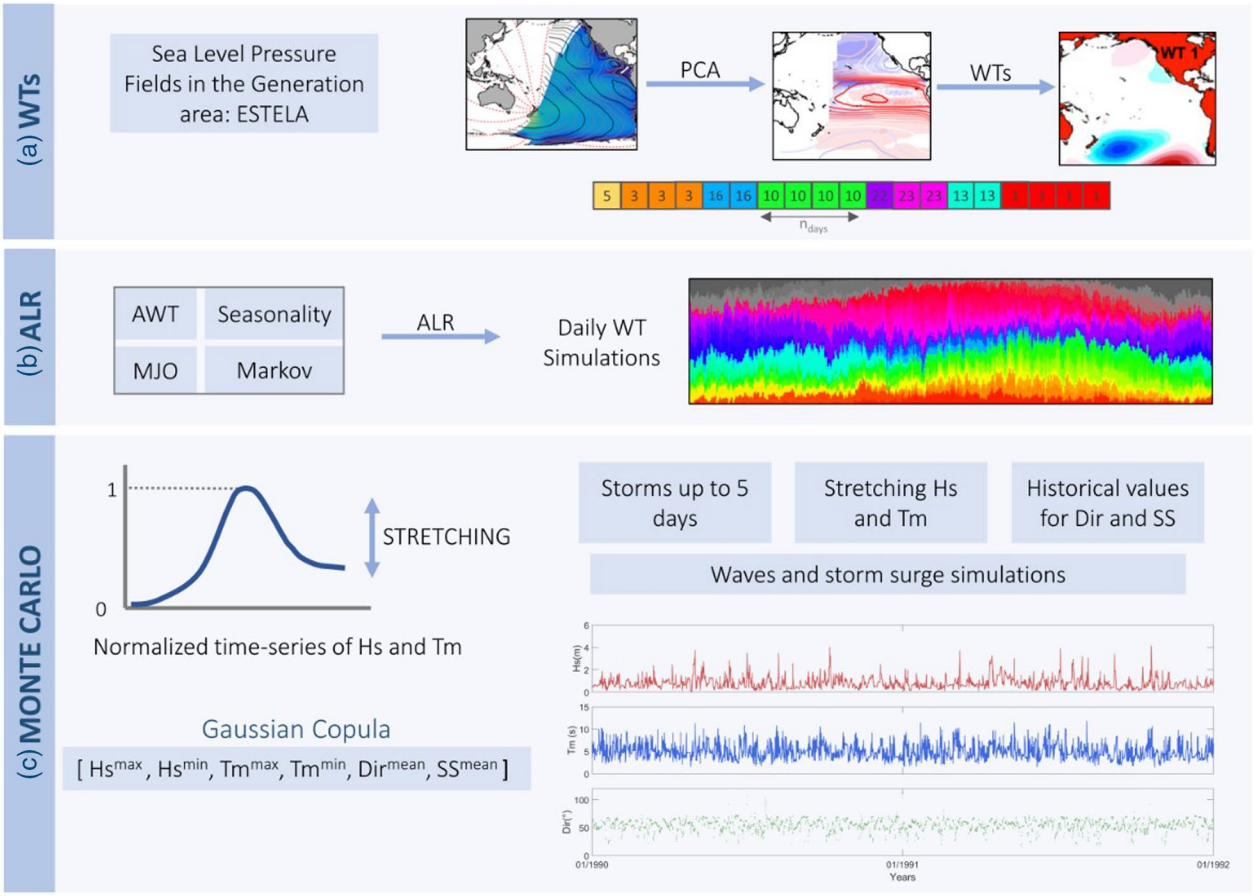

Figure 1. Methodology leading to 3-hourly realizations of wave climate following Cagigal et al. (2020): (a) Define historical daily Weather Types (WTs), based on sea-level pressure fields over the wave generation region, which is determined by the "Evaluating the Source and Travel of the wave Energy reaching a Local Area" (ESTELA)-method of Perez et al. (2014); (b) Reproduce sequences of daily WTs using an autoregressive logistic regression (ALR) model (Anderson et al., 2019); (c) Run Monte Carlo simulations to obtain wave parameters (e.g., wave height, wave period and wave direction) associated to each synoptic state. To account for the joint probability between variables, we use a multivariate Gaussian copula within each WT (Rueda et al., 2017).

in Figure 2 panels a–c. Here, we compare the probabilities associated to the hindcast (background grid) with the ones associated to the simulations (circles). A perfect match of the bivariate distributions between hindcast and simulation would be found when both the grid and the circle have the exact same probability (or the same color in Figure 2). As shown on Figure 2, we find a good, general agreement among the different parameters, although small differences could be found in some grids associated with small wave period (T_m) and wave height (H_s) values. In order to evaluate the extreme value distribution of the wave parameters, we compare the return periods for the (simulated and historical) wave height and wave period, shown in the middle and lower panels of Figure 2, respectively. The red line corresponds to the mean of the 1,000 simulations, the shaded areas represent the 95% confidence intervals and the dots are the historical values in the period 1979–2016. Once again, the simulated extreme wave conditions, which are critical to characterize the largest storm-driven erosion events, agree well with historical extreme wave data. The wave model of Cagigal et al. (2020) is capable of capturing the climate-driven changes in wave height expected before the end of the 21st (see e.g., Morim et al., 2019) by adjusting the occurrence probabilities of the model's underlying "weather types." However, for the current application, we simply assume a stationary wave climate that is consistent with historical conditions.

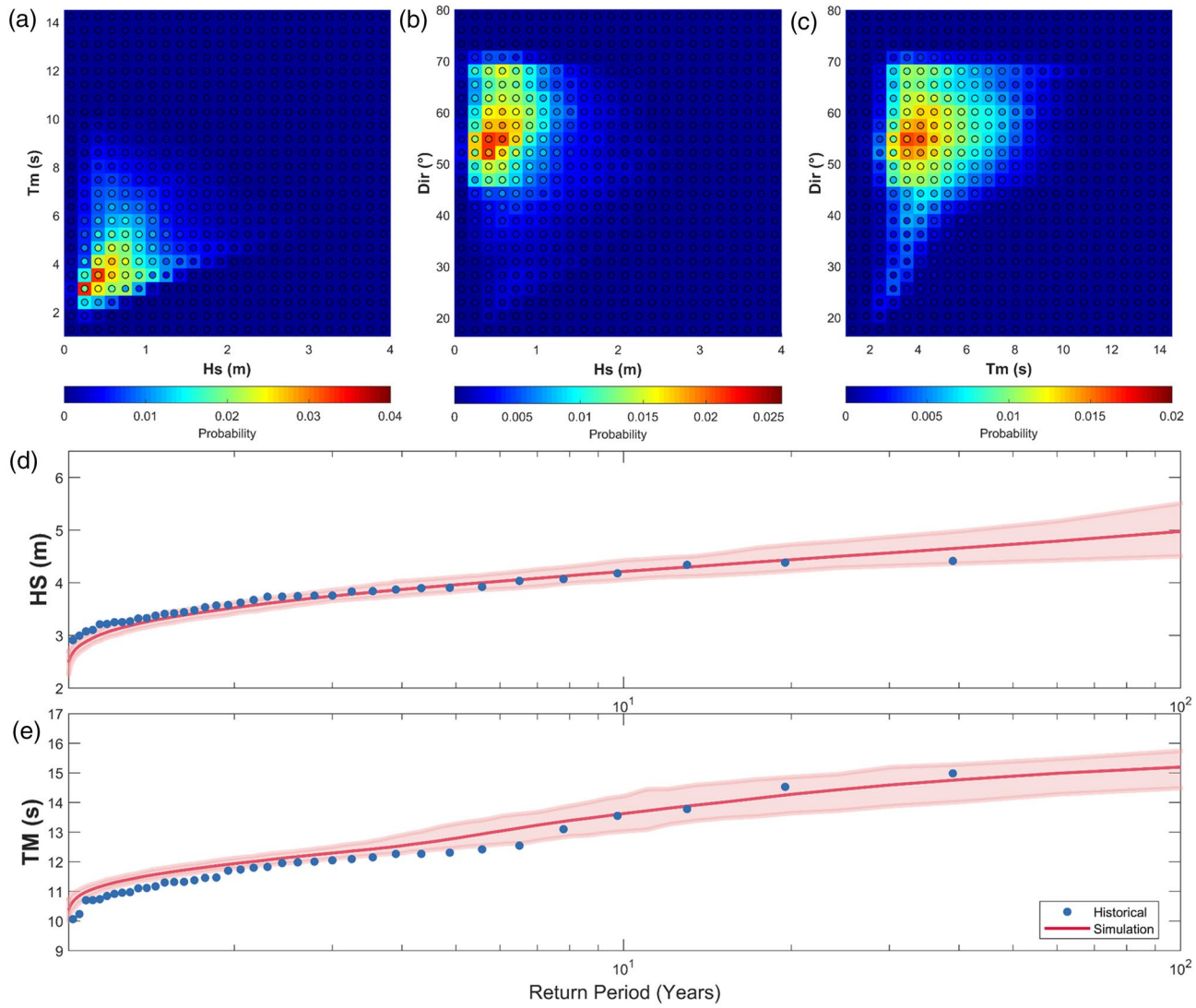

Figure 2. Validation of the simulated wave parameters against the historical data. Panels a, b, and c show comparisons of the probability of occurrence in the bivariate wave parameter space. The background grid color corresponds to the probability associated with the hindcast and colors of the circles correspond to the probability associated with the simulations. Panels d and e show wave height versus return period and mean wave period versus return period, respectively, for the hindcast (blue dots) and simulations (red solid lines with pink uncertainty limits).

3. Results

We present two contrasting simulations (with and without ensemble wave forcing) of Tairua beach, New Zealand modeled with the modified Yates et al. (2009) model, Equations 5–7. Here, we primarily focus on the short-term, cross-shore equilibrium shoreline response to waves (using Equations 5–7) as it dominates the observed record at Tairua beach (Blossier et al., 2017a, 2017b; van de Lageweg et al., 2013). For simplicity, we model the evolution and uncertainty of the alongshore-averaged shoreline position, and, hence, we ignore the effects of longshore transport. However, Montaño et al., 2020 showed that models that included both longshore and cross-shore sediment transport at Tairua beach did not show an improvement in the shoreline hindcast over short (multiyear) time scales compared to those that only included cross-shore processes.

The first ensemble simulation (shown in Figure 3) applies uniform wave-forcing conditions to each member of the $N_{ens} = 1{,}000$ ensemble. In other words, the same wave time series is applied to each member of the ensemble (although each ensemble member has different values of the model parameters and different

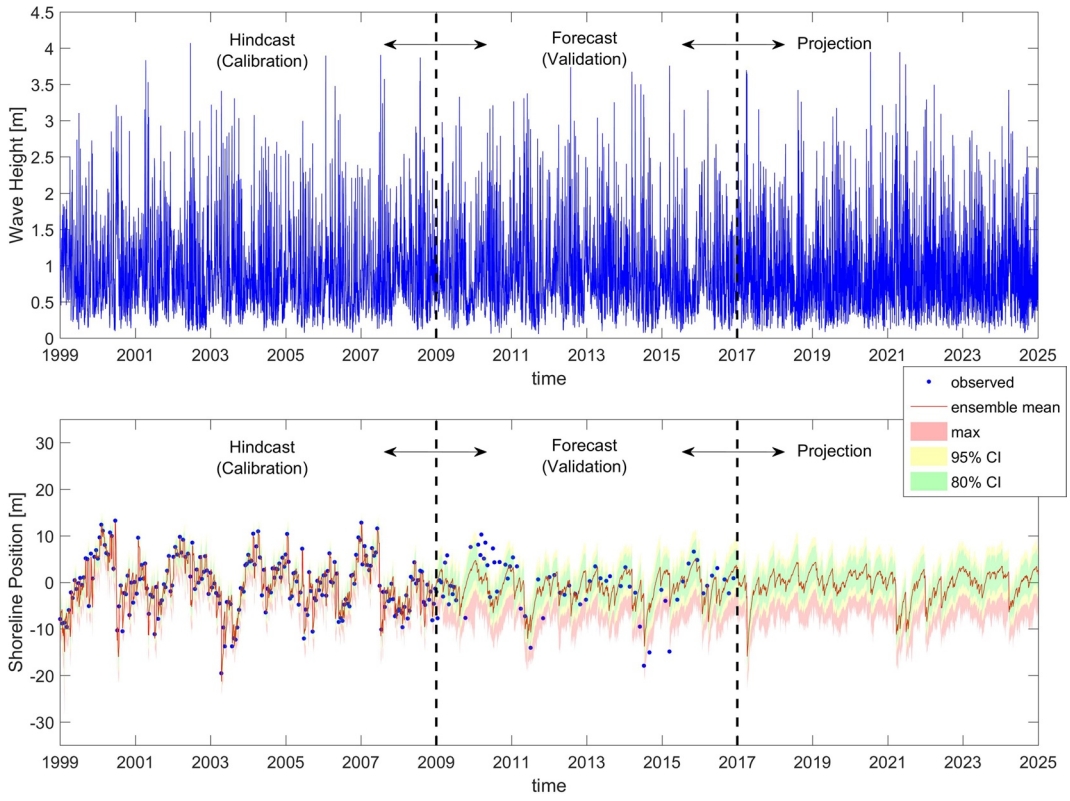

Figure 3. A $N_{ens} = 1{,}000$ ensemble shoreline simulation with uniform wave forcing (i.e., a single time series of wave conditions), shown on the top panel. The model is assimilated with observations (blue dots on the bottom panel) prior to 2009 during the "Hindcast (Calibration)" period. Data assimilation is turned off during the "Forecast (Validation)" period. No shoreline observations exist for model comparison during the "Projection" period, which starts in 2017. The bottom panel shows time series of the model's ensemble mean (red line) as well as 80% (green band) and 95% confidence intervals (yellow band) and the so-called "max" band (in red) between the 95% confidence level and the maximum eroded shoreline position across the entire ensemble.

realizations of the additive noise). The second ensemble simulation (shown in Figure 4) applies unique wave time series to each member of the ensemble. As detailed below, both simulation ensembles consider a range of the "best-guess," initial estimates of the model parameter values. Naturally, when best-guessing model parameter values, it is highly beneficial to have a model formulation based on parameters with physically intuitive dimensions as this facilitates assessment of an appropriate scale (or order of magnitude) for a given parameter. However, a modest mis-specification of the initial parameter ensemble (e.g., one that is approximately within an order of magnitude spread of the optimal value) generally does severely denigrate the assimilated parameter estimates over time (Evensen, 2003).

Figure 5 compares the model uncertainty, given by the square root of the variance of the shoreline position across the $N_{ens} = 1{,}000$ member ensemble, for the simulations shown in Figures 3 and 4. Each simulation is partitioned into three time periods representing (1) a 10-year data-assimilated "Hindcast (Calibration)" period, which assimilates data from 1999 to 2008, (2) an 8-year "Forecast (Validation)" period from 2009 to 2016 where observed wave and shoreline data exist but data assimilation is turned off, and (3) a "Projection" period (2017 and later) where no shoreline data are available for comparison, and where wave conditions are considered to be unknown. Hence, the ensemble wave-forcing conditions are applied only for the "Projection" period since the *actual* wave conditions (and resulting shoreline change) prior to 2017 are considered to be known in this example. For projections where neither shoreline nor wave observations exist (e.g., future projections), ensemble wave forcing conditions, in general, must be applied when the waves are considered unknown in a deterministic sense despite exhibiting consistent seasonal and interannual patterns in a statistical sense.

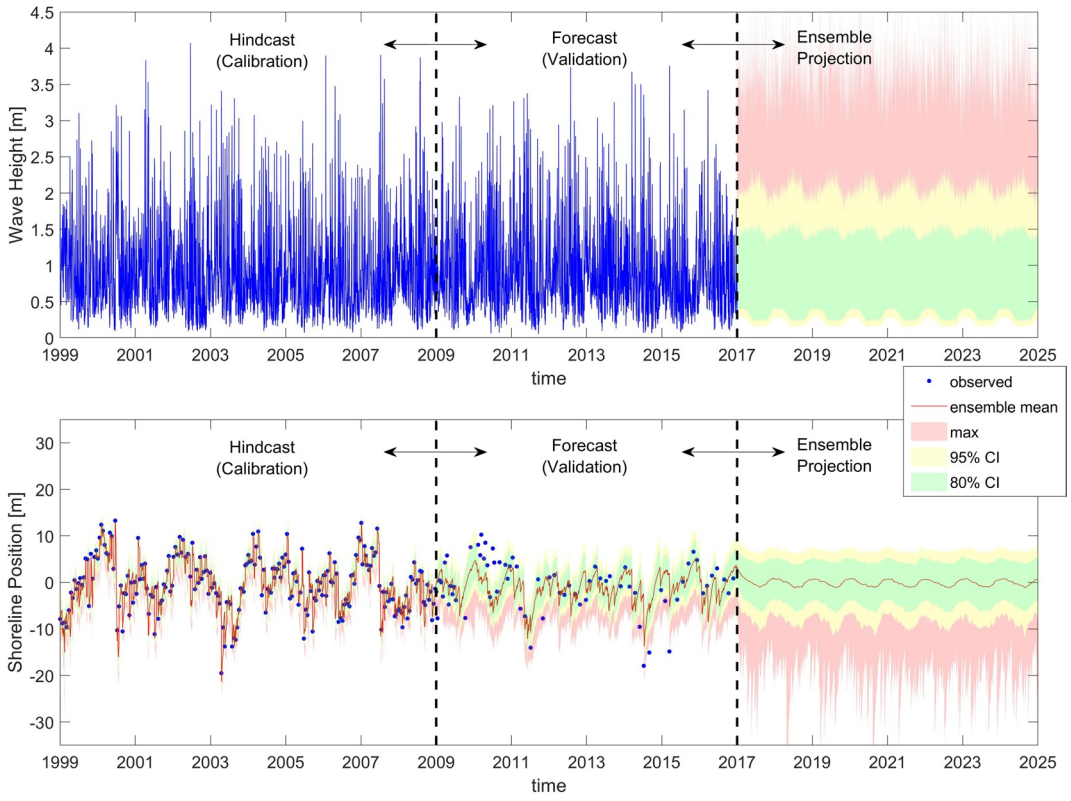

Figure 4. A $N_{ens} = 1{,}000$ ensemble shoreline simulation with ensemble wave forcing (i.e., a unique time series of wave conditions applied to each member of the shoreline model ensemble) applied during the "Ensemble Projection" period shown on the top panel. The model is assimilated with observations (blue dots on the bottom panel) prior to 2009 during the "Hindcast (Calibration)" period. Data assimilation is turned off during the "Forecast (Validation)" period. No wave or shoreline observations data exist for model comparison during the projection period, which starts in 2017. Hence, ensemble wave forcing conditions are used during the "Ensemble Projection" period when the waves are considered unknown in a deterministic sense, despite exhibiting consistent seasonal cycles in wave height in a statistical sense. The panels show time series of the model's ensemble mean (red line) as well as 80% (green band) and 95% confidence intervals (yellow band) and the so-called "max" band (in red) between the 95% confidence level and the maximum wave height (top panel) and maximum eroded shoreline position (bottom panel) across the entire ensemble.

The numerical solution to the governing equation used in the simulations presented here is given in Equation 22 with a time step of $\Delta t = 3$ hours. The original numerical method must be modified (without loss of form) to Equation 26 to ensure that the data-assimilation procedure maintains the expected signs of the model parameters as discussed above. In this example, the important model parameters are ΔT (the equilibrium shoreline adjustment time scale), ΔY (the equilibrium shoreline excursion), and $\hat{H}_s$ (the equilibrium wave height), as discussed above. The ensemble simulations here apply $N_{ens} = 1{,}000$, where each ensemble member differs in the values of its initial parameters and in the time series of its wave-forcing conditions (in the case shown in Figure 4). The $N_{ens} = 1{,}000$ model parameters are initialized with normally-distributed random-number generator with $\overline{\Delta T} = 28$ days, $\sigma_{\Delta T} = 1$ day, $\overline{\Delta Y} = 10$ m, $\sigma_{\Delta Y} = 2$ m, and $\overline{\hat{H}_s} = 0.8$ m (which is calculated from the mean wave-height time series) and $\sigma_{\hat{H}_s} = 0.166$ m (which is selected as 20% of $\overline{\hat{H}_s}$, based on our judgment as a reasonable initial spread of this parameter), where the overbar indicates the mean of the parameter and $\sigma_{\Delta T}, \sigma_{\Delta Y}$, and $\sigma_{\bar{H}_s}$ represent the standard deviations of the initial parameters ΔT, ΔY, and $\hat{H}_s$, respectively.

The simulations here apply additive noise of $\boldsymbol{\varepsilon} \sim \mathcal{N}\left(0, \sigma^2 = (0.2\,\mathrm{m})^2\right)$ at each time step, but only to the model solution Y (and not to the other model parameters ΔT, ΔY, and $\hat{H}_s$). Here, the prescribed additive noise (with a standard deviation of $\sigma = 0.2$ m) is a tunable parameter that we chose specifically to capture the deviations of the observations about the ensemble mean, as discussed below. The shoreline observation

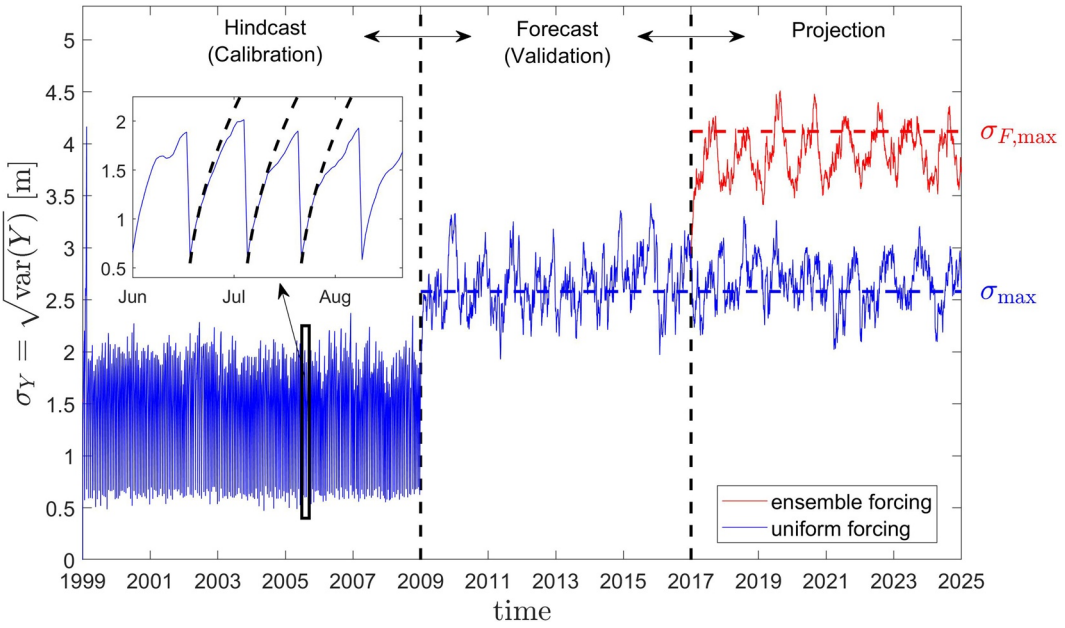

Figure 5. Comparison of the model uncertainty over time between the ensemble simulations shown in Figure 3 (in blue) and Figure 4 (in red). The figure cutout in the upper left corner depicts the growth of uncertainty compared to the theoretical (square-root time) growth rate given in Equation 31 of Appendix A (i.e., the black dashed line) that occurs following data assimilation steps. The uncertainty of the uniformly forced ensemble simulations (in solid blue) stabilizes near the theoretically derived value of $\sigma_{\max}$ from Equation 15, shown in the blue dashed line. The uncertainty of the ensemble wave forcing simulations (in solid red) stabilizes near the theoretical value of $\sigma_{F,\max}$ in Equation 13 with $F \approx 15$, shown in the red dashed line. Note that the standard deviation of the ensemble wave-forcing simulations, i.e., the 'uncertainty', is about 1–2 meters larger than the uniformly forced simulations, in this example.

error, used to calculate the Kalman gain in Equation 18, is set to $\sigma_{\mathrm{obs}} = 0.5\,\mathrm{m}$, which is consistent with the rectified pixel size of the imagery from van de Lageweg et al. (2013), which is used to derive the shoreline data at Tairua beach.

The $N_{\mathrm{ens}} = 1{,}000$ model ensemble uses a single wave time series for the simulations shown in Figure 3, despite the "true" future wave conditions after 2017 being considered unknown. In the ensemble projection shown in Figure 4, for each of the $N_{\mathrm{ens}} = 1{,}000$ ensemble members, we apply unique wave time series generated from the statistical downscaling method described above. However, in general, there is no requirement that a unique wave time series must be applied to each of the $N_{\mathrm{ens}} = 1{,}000$ members of the ensemble. In certain cases, it may preferable that the number of forcing conditions $N_f < N_{\mathrm{ens}}$, in the case where the ensemble wave conditions are computationally expensive to generate. In such cases (which is not the case here), certain ensemble members may utilize the same time series of wave conditions, albeit with different values of the model parameters (e.g., ΔT, ΔY, and, $\hat{H}_s$). As one might reasonably expect, we find that increasing the number of unique forcing conditions, N_f, increases the intrinsic uncertainty (although this analysis is not shown). For the current application, we find that a number of unique forcing conditions $N_f >\sim 250$ is sufficient for convergence of the intrinsic uncertainty (due to the convergence of the variance of the ensemble wave-height time series).

The top panels of Figures 3 and 4 show the hindcasted wave height time series at Tairua beach. In the top panel of Figure 4, the wave height transitions from a single time series to an ensemble after 2017, where time series of the 80% and 95% confidence intervals and ensemble maxima wave heights are depicted. The bottom panels of Figures 3 and 4 show time series of the 80% and 95% confidence intervals and the ensemble mean and maximum eroded shoreline positions (driven by the wave conditions in the top panel), where negative and positive values of the shoreline position (Y) represent eroded and accreted beach states, respectively. The confidence bands (in green, yellow, and red) are shown in the bottom panels of Figures 3 and 4, yet they only become visible when data assimilation is turned off at the start of the "Forecast (Validation)" period. During the "Hindcast (Calibration)" period, the confidence bands on Figures 3 and 4 are imperceptibly nar-

row, but the uncertainty levels can be seen in Figure 5. While data assimilation is turned on, each member of the model ensemble is nudged toward the synoptic observation data (i.e., the blue dots on the bottom panels of Figures 3 and 4), which represent the observed shoreline positions at Tairua beach at approximately bi-monthly intervals. During the "Forecast (Validation)" period when data assimilation is turned off, the widths of the confidence intervals (i.e., the difference between the upper and lower confidence bounds) appear relatively constant in time despite variations in the ensemble mean. This finding is also apparent in the consistency of the model uncertainty with time shown in Figure 5, as discussed below.

The variance in the model ensemble during the "Forecast (Validation)" period is primarily associated with the additive noise to the ensemble. A salient feature of the equilibrium shoreline model based on Yates et al. (2009), used here, is that even though noise is constantly being added to the shoreline position every time step, the confidence bounds do not appear to grow with time, as discussed in the following section. During the "Ensemble Projection" period in Figure 4, the variance in the model ensemble is due to the sum of the variance contributed by the additive noise and the variance introduced by the ensemble wave forcing conditions.

Figure 5 compares the evolution of model uncertainty between the ensemble simulations shown in Figure 3 (in blue) and Figure 4 (in red). The cutout in the upper left corner of Figure 5 depicts the growth of uncertainty following data-assimilation steps compared to the theoretical (square-root time) growth rate given in Equation 31 of Appendix A (i.e., the black dashed line). Note that the lower bound of the uncertainty in Figure 5 occurs immediately following a data-assimilation step and is consistent with that of the prescribed error in the shoreline position, $\sigma_{\text{obs}} = 0.5\,\text{m}$. When data assimilation is turned on, the model's confidence bands typically have standard deviations in the range $\sigma_Y = 0.5 - 2\,\text{m}$ (see Figure 5). As discussed in the following section, the uncertainty of the uniformly forced ensemble simulations (in solid blue) stabilizes near a value of $\sigma_{\max}$, given in Equation 15 and shown in the dashed blue dashed line in Figure 5. The uncertainty of the ensemble wave forcing simulations (in solid red) stabilizes near a value of $\sigma_{F,\max}$ given in Equation 13, which is shown in the dashed red dashed line in Figure 5. As shown in Figure 5, the standard deviation of the ensemble wave forcing simulations, that is the "uncertainty," is about 1–2 meters larger than the uniform forcing simulations in this example at Tairua beach, as a result of the ensemble wave forcing. Figure 5 exhibits temporally varying perturbations to the model variance, which cause it to differ from the theoretical result, due to variations in the wave height across the ensemble. Higher values of the fluctuations in the model uncertainty, in the case of the uniformly forced ensemble, are generally associated with smaller wave heights, because during these periods there is a large spread across the shoreline position ensemble. During the largest erosion events (e.g., post-2011 and just prior to 2015) in the "Forecast (Validation)" period, nearly all ensemble members are in an eroded state and thus the modeled uncertainty is generally near its minimum value. On the other hand, during the "Ensemble Projection" period, large spikes in shoreline variance of ensemble wave forcing simulations are generally associated with periods of larger variance in the wave forcing ensemble. For example, during the austral winter when the waves are largest. The variations in the model uncertainty, found here, are consistent with the results of D'Anna et al. (2020), who found that the variance-based contributions (i.e., sensitivity) of the equilibrium shoreline model parameters to shoreline change uncertainties vary strongly with in time, due to time variability in wave height.

The shoreline model simulations presented here require only 45 s of computer time on a 2.1 GHz workstation for a $N_{\text{ens}} = 1{,}000$ member ensemble for 26 years of simulation time. However, we note that the ensemble wave conditions, supplied as inputs to the shoreline model, are precomputed (because the wave model often represents the computational bottleneck). Thus, the limited computational cost of this model easily affords the potential for simulations of even larger ensembles or spatiotemporal extents.

4. Discussion

During the "Hindcast (Calibration)" period, the model applies data assimilation and thus the model solution and parameters are adjusted to fit the observations. Hence, agreement between the model and the observations during this period does not represent the skill of the model. However, we assess the model skill during the "Forecast (Validation)" period when data assimilation does not take place and the comparison between model and observations does indicate the model's skill in faithfully representing the ob-

served behavior. Note that, in general, the ensemble mean of the modeled shoreline position (red line in Figures 3 and 4) captures the interannual behavior of the observations during the "Forecast (Validation)," yet the agreement is not perfect. The model does not always perfectly capture the most eroded and most accreted states, although this issue persists for many shoreline models. Only the most eroded members of the ensemble come close to capturing the largest observed erosion events near 2015, which may be due to imperfections in the wave forcing time series, the model's parameters, and/or the model's physics.

The observations generally exhibit more noise than the smoother ensemble mean (red line in Figures 3 and 4) during the "Forecast (Validation)" period. The confidence bounds of the ensemble generally capture the slight, noisy offsets between model and observations, which likely result from unresolved processes like the tide, beach cusps, sand waves, longshore transport, etc. However, this occurrence is not fortuitous or coincidental, it is by design. The magnitude of user-prescribed additive noise, which controls the size of the uncertainty bounds (see Equation 15), is tuned to best capture the observations.

Reeve et al. (2014) state that "verifying the results of Monte Carlo simulation can be problematic because Nature only gives us one realization." To build upon this statement, we propose that ensemble simulations can sometimes make verification easier but also can make it trivial. For example, if the confidence bounds of ensemble simulations are not well constrained (e.g., due to forcing or additive noise, etc.), then it becomes trivial for future observations to fall within the model's bloated confidence bounds. This, of course, represents an unreasonably "low bar" for verification. Certainly, the predictability of strongly forced systems will be inherently limited without knowledge or constraint of nature's "actual" forcing conditions. However, when seeking to model an intrinsically noisy system with "known" antecedent forcing conditions, an ensemble modeling approach may provide a great benefit over a more dogmatic approach to the model parameters. For example, specifying a single, unchanging value of a model parameter to capture a wide range of system dynamics may not be entirely realistic. This notion especially pertains to the field of sediment transport, where important, yet unknown parameters abound. The value of ensemble modeling is perhaps most evident in the "Forecast (Validation)" period of Figures 3 and 4: it appears that the confidence bands (representing additive noise and the spread of the model parameters) can nicely capture the deviations between the ensemble mean and the single observed (realized) shoreline position. However, the agreement between model confidence bands and the fluctuations of the observations about the ensemble mean is only accomplished via the knowledge that the additive noise controls the size of the uncertainty bands and tuning its magnitude accordingly, as discussed below.

A salient feature of the confidence bands shown in Figures 3 and 4 (which is also evident in Figure 5) is that they remain roughly of constant width through time even though noise is constantly being added to the shoreline position. The near constant width of the uncertainty bands is noticeable in Figure 3 during the "Forecast (Validation)" and "Projection" periods, and is even more evident in Figure 4 during the "Ensemble Projection" period. Ignoring the red confidence bands (between the 95% confidence level and the ensemble maximum), the green and yellow confidence bands at the 80% and 95% confidence levels, respectively, are roughly constant with a slight seasonal oscillation. Upon initial impression, the apparent seasonal cycle of the "Ensemble Projection" period in Figure 4 seems muted compared with the seasonal cycle of the "Hindcast (Calibration)" and "Forecast (Validation)" periods. For example, the seasonal shoreline excursion of ensemble mean of the "Ensemble Projection" is only about ±1.0m from the background state compared with about ±10.0m during the prior periods. However, closer inspection reveals that large shoreline fluctuations during the "Hindcast (Calibration)" and "Forecast (Validation)" periods are driven by interannual fluctuations in the single time series of wave forcing rather than seasonal variations. The interannual variability during in the "Ensemble Projection" period is practically undetectable because the entire model ensemble experiences several different and possibly opposing realizations of interannual variability in the wave height.

A peculiar benefit of the "Ensemble Projection" is that it simultaneously captures both the extremes and the ordinary. The variation within the bounds of these two end-members becomes somewhat inscrutable when confidence bands are applied to the ensemble mean, unless some gradation (e.g., green, yellow, and red bands) is used. Overall, Figure 4 nicely illustrates the mirror-like reflection of the consistent pattern of the confidence bands in the wave forcing conditions (on the top panel) to the shoreline response (on the bottom panel) during the "Ensemble Projection" period. Below, we discuss the specific reasons for the

constant/consistent form of the confidence bands in the following discussion of Figure 5. Although one might reasonably expect a growing uncertainty or an increase in the width of the confidence bands with time (especially since noise is constantly being injected into the solution), this is not the case due to the behavior of the equilibrium shoreline model used here. Long-term processes such as longshore transport (e.g., beach rotation), sea-level rise, and sediment supply would certainty contribute to a growing uncertainty over longer periods of time, but these processes are not considered in the present analysis. The current equilibrium shoreline modeling approach could also capture the effects of long-term changes in wave climate (which are not modeled here) by establishing a new shoreline baseline state and new confidence limits.

Figure 5 shows a time series of the model uncertainty, given by the square root of the variance of the model ensemble at the current time step. The uncertainty during the "Hindcast (Calibration)" period is low compared with the "Forecast (Validation)" period and the "Projection" period due to the data assimilation procedure, which adjusts the model state to best fit the observations. During the "Hindcast (Calibration)" period, the uncertainty resembles a sawtooth pattern with minima of approximately 0.5 m, which is the standard deviation of the prescribed, normally distributed noise associated with the observations, σ_{obs}. Immediately, following the data-assimilation step, which adjusts the model state to resemble that of the observations, the ensemble variance grows linearly with time, and thus the uncertainty grows like the square root of time as demonstrated in Appendix A. The cutout in Figure 5 shows a zoomed-in plot of a few months of the simulation and compares the model uncertainty to the theoretical (square-root time) growth rate given by Equation 31 of Appendix A. Here, the good agreement between the modeled and theoretical rates of growth in the uncertainty indicates that the magnitude of the (prescribed) additive noise to the model state ($\varepsilon \sim \mathcal{N}\left(0, \sigma^2 = (0.2\,\text{m})^2\right)$) is responsible for the behavior of the model uncertainty during the data-assimilation period, since the additive noise directly controls the growth rate via Equation 31 of Appendix A. Eventually, the modeled uncertainty diverges from the theoretical growth rate because the uncertainty begins to asymptote to the background level of σ_{max} (determined by the theoretical result in Equation 15), which is achieved through the balance between the additive noise to the model state and the process of damping governed by the equilibrium shoreline change model. The roughly constant background value of the model uncertainty is never reached during the data-assimilation period because the next data-assimilation step occurs and nudges all of the members of the model ensemble back to the observed shoreline position. Hence, the variance growth rate is, in this case, not sufficient to allow the model uncertainty to grow long enough to reach the new background level (e.g., Equation 15) before the next data-assimilation step takes place. However, during the "Forecast (Validation)'" period when data assimilation is turned off, the model uncertainty roughly approaches the background level of σ_{max} (Equation 15) given by the blue dashed line on Figure 5. It is important to note that the user-prescribed additive noise levels, that is, $\varepsilon \sim \mathcal{N}\left(0, \sigma^2 = (0.2\,\text{m})^2\right)$ appear to dominate the epistemic uncertainty. It is perhaps somewhat unsatisfying that tunable parameters (i.e., "knobs") remain despite the application of a state-of-the-art parameter estimation (i.e., the ensemble Kalman Filter). However, we have clearly demonstrated the role of the additive noise "knob" in setting the background epistemic uncertainty, which (at the very least) is consistent with the notion that epistemic uncertainty represents the user-controlled "knowledge limits" of the model. Hence, the processes that contribute most to the model's epistemic uncertainty *should be* "tunable." Accordingly, a best practice for conducting ensemble simulations might be to adjust the additive noise levels until the (epistemic) uncertainty bands capture the variability of the observations about the ensemble mean. This practice, of course, seems to necessarily require (a reasonably complete set of) observations. Hence, it may be possible that the additive noise might be calibrated automatically (e.g., via data assimilation) rather than manually, as is the case here, although this is beyond the scope of the current research. Finally, after the tuning practice is completed, the intrinsic uncertainty can be assessed when the model user applies ensemble forcing conditions while holding fixed the epistemic uncertainty.

During the "Ensemble Projection" period in Figure 5, the model uncertainty once again exhibits a roughly constant background value. The background uncertainty level is consistent with the theoretical value of $\sigma_{F,\text{max}}$ (Equation 13), which is determined via the sum of the epistemic uncertainty due to the additive noise and intrinsic uncertainty due to the ensemble wave forcing. The theoretical result in Equation 13 accounts for the covariance of the ensemble wave forcing conditions with time via a factor F, which has the effect of increasing the model variance compared with a random forcing function (see Appendix A

Equations 80–84). In this case, the factor $F \approx 15$ for the wave ensemble at Tairua beach, which is determined by the ratio between the sum off diagonal elements to the sum of the diagonal elements of the covariance matrix of the ensemble wave time series, as given in Equation 14. Physically, F represents the ratio of the covariance of the wave forcing ensemble with time to the variance of the ensemble at an instant in time. Hence, large values of F indicate high degrees of covariance or correlation of the forcing ensemble with time, which is certainly the case for physical processes like wave height. Consequently, large values of F increase the overall model uncertainty, since the shoreline state evolves in concert with the (auto-correlated) wave forcing. For different model formulations, locations, or periods of interest, the value of the factor F may differ from the result presented here, however it can be easily calculated directly from an ensemble time series of forcing conditions via Equation 14. Never-the-less, the role of the factor F emphasizes the importance of properly characterizing ensemble storm sequences in the ensemble wave model.

In Figure 5, the agreement between the modeled and theoretical uncertainty is excellent for both the ensemble projections (e.g., $\sigma_{F,\max}$ from Equation 13) and for the uniformly-forced projections (e.g., $\sigma_{\max}$ from for Equation 15), which clearly demonstrates utility of the theoretical results derived from the idealized models presented in Appendix A.

In this application at Tairua beach, the intrinsic uncertainty due to the ensemble forcing function is approximately 50% more than that of the epistemic uncertainty, therefore the overall model variance (which represents the sum of the noise components) is approximately two and a half times larger for the ensemble projection (e.g., Figure 4) than for the uniform-forced projection (e.g., Figure 3). Hence, intrinsic uncertainty due to ensemble wave forcing conditions must be accounted for when seeking robust projections of future change. In cases where ensemble forcing is unavailable, the heuristic approach of doubling to tripling the uncertainty of the uniformly forced projections may suffice. However, the heuristic factor of increase in uncertainty will depend on the physical state of the beach of interest, its oceanographic forcing conditions, and the important feedbacks between beach state and hydrodynamic processes (e.g., Wright & Short, 1984). Yet, the analytical results presented here, e.g., using Equations 13–15, may help to characterize the unresolved contributions to uncertainty when applying single realization simulations of shoreline change.

5. Conclusions

We present an ensemble Kalman filter shoreline change model to predict short- and long-term shoreline change driven by waves. The ensemble simulations presented here facilitate both data assimilation and uncertainty quantification in a straightforward manner. Further, ensemble simulations motivate the use of multiple realizations of future wave conditions to force model projections of coastal change. Ensemble forcing conditions are key to develop robust shoreline change projections in cases where the wave conditions are unknown (deterministically), yet exhibit consistent patterns (e.g., seasonally and interannually) in a statistical sense. In this application, we demonstrate that the variance of the modeled shoreline position more than doubles when accounting for the intrinsic uncertainty of future wave climate (i.e., by utilizing ensemble wave forcing conditions).

The new approach to model uncertainty quantification, presented here, reveals the individual contributions of epistemic and intrinsic uncertainty across different processes and spatiotemporal scales. We demonstrate examples of how the ensemble variance/uncertainty of shoreline change models can be quantified via analytical relationships derived from ensembles of idealized process models. Overall, we find that the confidence bands of wave-driven, equilibrium shoreline change simulations (for Yates-type formulations but not for ShoreFor) are predictable: the model uncertainty rapidly approaches a roughly time-invariant background value determined by the sum of the epistemic uncertainty due to additive (i.e., user-prescribed) noise and the intrinsic uncertainty due to variance in the forcing of the system, which is modified by the damping (or equilibrium response) of the shoreline change model. This finding reveals a tight connection between stochastic wave forcing and shoreline response, which must be accounted for when seeking robust, uncertainty-aware projections of future change.

Appendix A: Uncertainty quantification of ensembles of idealized process models.

In this appendix, we analyze the behavior of ensembles of idealized, dynamical process models to inform the characteristics of the uncertainty/variance of more complex shoreline change models, like Yates et al. (2009), detailed above. However, the idealized models investigated here apply to a wide range of ensemble modeling practices throughout different fields. Here, we consider idealized models that include the processes of forcing, damping, and noise, as given below

$$\frac{dY}{dt} = \underbrace{\frac{1}{\Delta T_f} f(t)}_{[1]\ \text{forcing}} - \underbrace{\lambda_\tau Y}_{[2]\ \text{damping}} + \underbrace{\varepsilon}_{[3]\ \text{noise}}. \tag{29}$$

Appendix A presents complete mathematical analyses and derivations of the uncertainty of idealized process models that include combinations of the right-hand side terms in Equation 29. The first case study presented below, a random walk ensemble (which analyzes the effect of only term [3] in Equation 29), is a "textbook" example (see e.g., Jones & Smith, 2017; Papoulis & Pillai, 2002) of the uncertainty of a (Gaussian) random walk, Brownian motion, or a Wiener process (which all demonstrate linear increases in variance with time). However, to our knowledge, the analytical estimates of the variance of the other idealized process models detailed below have not been presented before.

In the following analysis, we develop a hierarchy of models to predict the evolution of the variable Y, which, in this case, represents the shoreline position. Alternatively, Y could represent some arbitrary state of a system in any other application. We apply the following evolution models for the state variable Y in an ensemble:

$$\boldsymbol{Y} = \begin{bmatrix} Y_1 & Y_2 & Y_3 & \cdots & Y_{N_{\text{ens}}} \end{bmatrix} \tag{30}$$

where N_{ens} is the number of ensembles. Here, each of the individual ensemble members of $\mathbf{Y}$ evolves according to the same underlying model, but with different forcing conditions, noise perturbations, model parameters, etc. In this appendix, we seek to analyze the propagation of uncertainty by deriving metrics that describe the evolution of the ensemble mean, $E(\mathbf{Y})$, and variance, $\text{var}(\mathbf{Y})$. In the following examples, we equate the model variance, i.e., $\text{var}(\mathbf{Y})$ (or the square root thereof) with the model uncertainty, while acknowledging that in practice there are more sources of uncertainty (such as those not resolved by the underlying model) that are not considered here.

Summary

The analysis presented in Examples 1–5 below involve lengthy mathematical derivations of the uncertainty of idealized process models for the highly motivated reader. Hence, for clarity, we begin with a brief summary of the major findings of Examples 1–5 below (Table 2).

Below, we enumerate the major findings of the uncertainty analysis derived in Appendix A:

1. Example #1: The variance of an ensemble random walk ($\mathbf{Y}^{n+1} = \mathbf{Y}^n + \boldsymbol{\varepsilon}^n$) with sequential Gaussian, 'white-noise' perturbations of $\boldsymbol{\varepsilon} \sim \mathcal{N}(0, \sigma^2)$ grows linearly with time (see Equation 49 and Figure 6 of Appendix A) according to the formula

$$\text{var}\left(\mathbf{Y}^N\right) = \sigma^2 N = \sigma^2 \frac{t}{\Delta t}, \tag{31}$$

which is derived in Equation 49 of Appendix A and is repeated here for clarity. This is a "textbook" example (see e.g., Jones & Smith, 2017; Papoulis & Pillai, 2002) of a (Gaussian) random walk, Brownian motion, or a

Table 2
Uncertainty of Ensembles of Idealized Process Models (Derivations Can Be Found in the Following Examples in Appendix A)

Model	Model equation	Variance equation (i.e., $\mathrm{var}\left(\mathbf{Y}\right)$ after N time steps)	Variance behavior
Noise (Random Walk)	$\mathbf{Y}^{n+1} = \mathbf{Y}^n + \boldsymbol{\varepsilon}^n$ (Equation 40) where $\boldsymbol{\varepsilon} \sim \mathcal{N}\left(0,\sigma^2\right)$ is random (white) noise	$\mathrm{var}\left(\mathbf{Y}^N\right) = \sigma^2 N = \sigma^2 \frac{t}{\Delta t}$ (Equation 49)	Variance grows linearly with time
Noise + Damping	$\mathbf{Y}^{n+1} = \lambda \mathbf{Y}^n + \boldsymbol{\varepsilon}^n$ (Equation 51) where $\lambda = 1 - \Delta t \,/\, \Delta T < 1$, Δt = model time step, ΔT = damping time scale.	$\mathrm{var}\left(\mathbf{Y}^N\right) \approx \left(\frac{\alpha}{\alpha - 1}\right)\sigma^2 = \sigma^2_{\max}$ (Equation 59) where $\alpha = \frac{1}{\lambda^2}$	Variance approaches $\sigma^2_{\max}$. Uncertainty bounded by $\sim \pm 3\sigma_{\max}$
Noise + Damping + (uniform) Forcing	$\mathbf{Y}^{n+1} = \frac{\Delta t}{\Delta T_f} f^n + \lambda \mathbf{Y}^n + \boldsymbol{\varepsilon}^n$ (Equation 61) the forcing f is uniform for the entire ensemble. ΔT_f = forcing time scale.	Same as above (i.e., the forcing does not contribute to the variance when it is applied uniformly across the entire ensemble)	Same as above
Noise + Damping + (random) Forcing	$\mathbf{Y}^{n+1} = \frac{\Delta t}{\Delta T_f} \mathbf{f}^n + \lambda \mathbf{Y}^n + \boldsymbol{\varepsilon}^n$ (Equation 61) where $\mathbf{f} \sim \mathcal{N}\left(0,\sigma_f^2\right)$ is a random forcing function.	$\mathrm{var}\left(\mathbf{Y}^N\right) \approx \left(\frac{\alpha}{\alpha - 1}\right)\left[\underbrace{\sigma^2}_{\text{variance from additive noise}} + \underbrace{\left(\frac{\Delta t}{\Delta T_f}\right)^2 \sigma_f^2}_{\text{variance from forcing}}\right] = \sigma^2_{f,\max}$ (Equation 71)	Variance approaches $\sigma^2_{f,\max}$. Uncertainty bounded by $\sim \pm 3\sigma_{f,\max}$
Noise + Damping + (general) Forcing	$\mathbf{Y}^{n+1} = \frac{\Delta t}{\Delta T_f} \mathbf{f}^n + \lambda \mathbf{Y}^n + \boldsymbol{\varepsilon}^n$ (Equation 75) where $\mathbf{f}$ is a general (auto-correlated) ensemble forcing function with variance $\mathrm{var}\left(\mathbf{f}\right) \approx \sigma_f^2$.	$\mathrm{var}\left(\mathbf{Y}^N\right) \approx \left(\frac{\alpha}{\alpha - 1}\right)\left[\underbrace{\sigma^2}_{\text{variance from additive noise}} + \underbrace{\left(\frac{\Delta t}{\Delta T_f}\right)^2 F\sigma_f^2}_{\text{variance from forcing}}\right] = \sigma^2_{F,\max}$ (Equation 84) where $F \approx 1 + \frac{\sum_{i \neq j} \mathrm{cov}\left(\mathbf{f}^i, \mathbf{f}^j\right)}{\sum_{i=1}^{N} \mathrm{var}\left(\mathbf{f}^i\right)}$. Here, $F \approx 15$.	Variance approaches $\sigma^2_{F,\max}$. Simulations are non-Gaussian and thus are not necessarily bounded by $\sim \pm 3\sigma_{F,\max}$

Wiener process. However, to our knowledge, the subsequent analyses of the variance of more complicated (but still idealized) models are original.

2. Example #2: The variance of an ensemble damped, random walk ($\mathbf{Y}^{n+1} = \lambda \mathbf{Y}^n + \boldsymbol{\varepsilon}^n$ where $\lambda < 1$) cannot grow indefinitely as it does in Equation 31 because it is suppressed by damping (see Figure 7 of Appendix A). The variance of an ensemble damped, random walk becomes approximately

$$\sigma^2_{\max} = \left(\frac{\alpha}{\alpha - 1}\right)\sigma^2, \tag{32}$$

which is derived in Equation 59 of Appendix A and is repeated here for clarity. In Equation 32, $\sigma^2_{\max}$ is set by the product of the variance of the additive noise (σ^2) and a coefficient related to damping, $\frac{\alpha}{\alpha - 1}$, which is generally larger than 1 (since $\alpha = \frac{1}{\lambda^2} > 1$ and $\lambda < 1$). Intuitively, increasing the amount of damping decreases the maximum variance $\sigma^2_{\max}$ and vice versa.

3. Example #3: The variance of an ensemble (randomly) forced, damped, random walk ($\mathbf{Y}^{n+1} = \frac{\Delta t}{\Delta T_f} \mathbf{f}^n + \lambda \mathbf{Y}^n + \boldsymbol{\varepsilon}^n$ where $\mathbf{f} \sim \mathcal{N}\left(0,\sigma_f^2\right)$) is still bounded, but is increased relative to that of the damped, random walk given in Equation 32. The variance of the sum of uncorrelated variables is the sum of their individual variances, according to the Bienaymé formula. For example, $\mathrm{var}\left(\mathbf{X} + \mathbf{Y}\right) = \mathrm{var}\left(\mathbf{X}\right) + \mathrm{var}\left(\mathbf{Y}\right)$ when $\mathbf{X}$ and $\mathbf{Y}$ are uncorrelated (i.e., $\mathrm{cov}\left(\mathbf{X},\mathbf{Y}\right) = 0$). Hence, in the context of a randomly forced, damped

random walk, the overall model variance represents sum of two variance terms contributed individually by the noise and the forcing terms that is approximately

$$\sigma_{f,\max}^2 = \left(\frac{\alpha}{\alpha - 1}\right)\left[\underbrace{\sigma^2}_{\text{variance from additive noise}} + \underbrace{\left(\frac{\Delta t}{\Delta T_f}\right)^2 \sigma_f^2}_{\text{variance from (random) forcing}}\right], \tag{33}$$

where the variance of the forcing term is given by $\text{var}(\mathbf{f}) = \sigma_f^2$. Equation 33 is derived in Equation 71 of Appendix A and is repeated here for clarity.

4. Example #4: The variance of an ensemble (generally) forced, damped, random walk ($\mathbf{Y}^{n+1} = \frac{\Delta t}{\Delta T_f}\mathbf{f}^n + \lambda \mathbf{Y}^n + \boldsymbol{\varepsilon}^n$) is still bounded, but differs slightly from Equation 33. For most geophysical models and applications, the forcing conditions will, in general, not be normally distributed. When the forcing conditions are not random, the covariance of the forcing ensemble generally increases the variance contributed by the forcing term. Thus, the overall variance of an ensemble (generally) forced, damped, random walk is approximately

$$\sigma_{F,\max}^2 = \left(\frac{\alpha}{\alpha - 1}\right)\left[\underbrace{\sigma^2}_{\text{variance from additive noise}} + \underbrace{\left(\frac{\Delta t}{\Delta T_f}\right)^2 F\sigma_f^2}_{\text{variance from (general) forcing}}\right], \tag{34}$$

which is derived in Equation 84 of Appendix A and is repeated here for clarity. Comparing Equations 33 and 34, notice that the factor F in Equations 34 acts to increase the variance contributed by a general forcing function compared to that of a random forcing function. This factor is given by

$$F \approx 1 + \frac{\sum_{i \neq j} \text{cov}\left(\mathbf{f}^i, \mathbf{f}^j\right)}{\sum_{i=1}^{N} \text{var}\left(\mathbf{f}^i\right)}, \tag{35}$$

which is derived in Equations 82–83 of Appendix A. In the current application, we find that the covariance of the forcing ensemble increases the variance of the forcing term by a factor of $F \approx 15$ compared to the case of random forcing conditions. Qualitatively, this increase makes sense: when the wave forcing conditions are auto-correlated, they will generally cause persistent changes (e.g., erosion or accretion) over the span of several time steps compared to random forcing conditions that may change sign every time step. Thus, the cumulative effect of the forcing on the model's state (and its variance) is increased.

5. Example #4 (continued): For Gaussian noise and forcing conditions, the simulations are nearly bounded by $\pm 3\sigma_{\max}$ or $\pm 3\sigma_{f,\max}$, meaning that ~99.7% of simulations will fall within this equilibrium range. For non-Gaussian (and potentially auto-correlated) forcing conditions, the variance still approaches $\sigma_{F,\max}^2$ on average (according to Equation 34). However, symmetric uncertainty limits, like $\pm 3\sigma_{F,\max}$, which originate from the assumption of Gaussian statistics, are generally not appropriate to describe the potential range of the non-Gaussian simulations (see Example #4 and Figure 11 of Appendix A for further details).

Example #5: The ShoreFor model, as demonstrated in Equation 90, can be written entirely in terms of a forced, ordinary differential equation of the form $\frac{dY}{dt} = \underbrace{f(t)}_{\text{wave forcing}}$. Hence, the uncertainty of the ShoreFor model does not approach a constant value, as in does in Examples 2–4 when a (shoreline-position-dependent) damping term is present.

The properties and behavior of the ensembles of idealized process models, discussed above (particularly that of Example #4), directly apply to the uncertainty of the shoreline change simulations (with and without ensemble wave forcing) presented in Results.

Example #1: Random walk ensemble

The first model we consider is a simple Gaussian random walk.

$$\mathbf{Y}^{n+1} = \mathbf{Y}^{n} + \boldsymbol{\varepsilon}^{n} \tag{36}$$

where

$$\boldsymbol{\varepsilon}^{n} = \begin{bmatrix} \varepsilon_1^n & \varepsilon_2^n & \varepsilon_3^n & \cdots & \varepsilon_{N_{\text{ens}}}^n \end{bmatrix} \tag{37}$$

is an ensemble of additive noise and

$$\varepsilon \sim \mathcal{N}\left(0, \sigma^2\right) \tag{38}$$

is a perturbation drawn from a normal distribution with zero mean and standard deviation σ.

In terms of a differential equation, Equation 36 can be written as:

$$\frac{dY}{dt} = \frac{\varepsilon}{\Delta t} \tag{39}$$

where Δt is equivalent to the model time step of the numerical method. A numerical model governing the evolution equation of Equation 39 can be written as

$$\frac{\mathbf{Y}^{n+1} - \mathbf{Y}^{n}}{\Delta t} = \frac{\boldsymbol{\varepsilon}^{n}}{\Delta t}$$

or

$$\mathbf{Y}^{n+1} = \mathbf{Y}^{n} + \boldsymbol{\varepsilon}^{n} \tag{40}$$

when the first-order, forward Euler time-stepping method (e.g., Moin 2010) is employed. Note that Equation 40 has been rearranged as an update equation that is of the same form as Equation 36.

Evaluating Equation 36 over the first few time steps, we see that noise accumulates over time:

$$\begin{aligned}
&\mathbf{Y}^{n+1} = \mathbf{Y}^{n} + \boldsymbol{\varepsilon}^{n} \\
&\mathbf{Y}^{1} = \mathbf{Y}^{0} + \boldsymbol{\varepsilon}^{0} = \mathbf{Y}^{0} + \boldsymbol{\varepsilon}^{0} \\
&\mathbf{Y}^{2} = \mathbf{Y}^{1} + \boldsymbol{\varepsilon}^{1} = \left(\mathbf{Y}^{0} + \boldsymbol{\varepsilon}^{0}\right) + \boldsymbol{\varepsilon}^{1} = \mathbf{Y}^{0} + \boldsymbol{\varepsilon}^{0} + \boldsymbol{\varepsilon}^{1} \\
&\mathbf{Y}^{3} = \mathbf{Y}^{2} + \boldsymbol{\varepsilon}^{2} = \left(\mathbf{Y}^{0} + \boldsymbol{\varepsilon}^{0} + \boldsymbol{\varepsilon}^{1}\right) + \boldsymbol{\varepsilon}^{2} = \mathbf{Y}^{0} + \boldsymbol{\varepsilon}^{0} + \boldsymbol{\varepsilon}^{1} + \boldsymbol{\varepsilon}^{2} \\
&\cdots
\end{aligned}$$

$$\mathbf{Y}^{N} = \mathbf{Y}^{N-1} + \boldsymbol{\varepsilon}^{N-1} = \mathbf{Y}^{0} + \boldsymbol{\varepsilon}^{0} + \boldsymbol{\varepsilon}^{1} + \boldsymbol{\varepsilon}^{2} + \ldots + \boldsymbol{\varepsilon}^{N-1} \tag{41}$$

$$\mathbf{Y}^{N} = \mathbf{Y}^{0} + \sum_{i=0}^{N} \boldsymbol{\varepsilon}^{i} \tag{42}$$

We can find the ensemble mean after a large number of time steps N, by taking the expected value of Equation 41, which is given by

$$E\left(\mathbf{Y}^N\right) = E\left(\mathbf{Y}^{N-1}\right) + E\left(\boldsymbol{\varepsilon}^{N-1}\right) = E\left(\mathbf{Y}^0\right) + E\left(\boldsymbol{\varepsilon}^0\right) + E\left(\boldsymbol{\varepsilon}^1\right) + E\left(\boldsymbol{\varepsilon}^2\right) + \ldots + E\left(\boldsymbol{\varepsilon}^{N-1}\right) \tag{43}$$

The expected value of the noise term is given by

$$E\left(\boldsymbol{\varepsilon}^0\right) \approx E\left(\boldsymbol{\varepsilon}^1\right) \approx E\left(\boldsymbol{\varepsilon}^2\right) \approx E\left(\boldsymbol{\varepsilon}^{N-1}\right) \approx 0 \tag{44}$$

according to Equation 38 since the noise is drawn from a normal distribution with zero mean. As in Equation 44, we use the approximately equal (≈) notation, because, in practice, a sample of computer-generated, normally distributed random numbers will not have an identically zero mean. If the expected value of the noise term were non-zero, this would create a 'drift' or trend in the random walk. As in Equation 43, the expected value of $\mathbf{Y}^N$ is the same as the expected value of the initial condition $\mathbf{Y}^0$, that is, $E\left(\mathbf{Y}^N\right) = E\left(\mathbf{Y}^0\right)$

Thus combining Equations 43 and 44 gives,

$$E\left(\mathbf{Y}^N\right) \approx E\left(\mathbf{Y}^0\right). \tag{45}$$

Assuming that the initial conditions of Y start from zero, i.e., $Y^0 = 0$, Equation 45 becomes

$$E\left(\mathbf{Y}^N\right) = 0. \tag{46}$$

Thus, the ensemble mean does not change in time, which is the case for the following two examples, which apply Gaussian perturbations with zero mean.

Taking the variance of Equation 41 gives

$$\begin{aligned} \mathrm{var}\left(\mathbf{Y}^N\right) &= \mathrm{var}\left(\mathbf{Y}^{N-1}\right) + \mathrm{var}\left(\boldsymbol{\varepsilon}^{N-1}\right) = \mathrm{var}\left(\mathbf{Y}^0\right) + \mathrm{var}\left(\boldsymbol{\varepsilon}^0\right) + \mathrm{var}\left(\boldsymbol{\varepsilon}^1\right) + \mathrm{var}\left(\boldsymbol{\varepsilon}^2\right) + \ldots + \mathrm{var}\left(\boldsymbol{\varepsilon}^{N-1}\right) \\ &= \mathrm{var}\left(\mathbf{Y}^0\right) + \sigma^2 + \sigma^2 + \sigma^2 + \ldots + \sigma^2 \\ &= \mathrm{var}\left(\mathbf{Y}^0\right) + \sigma^2 N \end{aligned} \tag{47}$$

since the variance of each perturbation ensemble, $\boldsymbol{\varepsilon}^n$, is independent and is given by

$$\mathrm{var}\left(\boldsymbol{\varepsilon}^n\right) = \sigma^2 \tag{48}$$

according to Equation 38 since the noise is drawn from a normal distribution with a standard deviation of σ.

Assuming that the initial conditions of Y once again start uniformly from zero, that is, $Y^0 = 0$, Equation 47 becomes

$$\mathrm{var}\left(\mathbf{Y}^N\right) = \sigma^2 N = \sigma^2 \frac{t}{\Delta t} \tag{49}$$

where $N = \frac{t}{\Delta t}$ is the number of time steps taken.

For the idealized simulations presented here, we apply $N_{\mathrm{ens}} = 10{,}000$ member ensembles due to their computational affordability, which greatly exceeds that of the realistic, ensemble simulations (with $N_{\mathrm{ens}} = 1{,}000$) presented in Results. Figure 6 illustrates an ensemble simulation of the random walk governed by Equation 40 with $N_{\mathrm{ens}} = 10{,}000$, $\sigma = 0.1$, and $\Delta t = 0.1$. Note that in the following examples we treat all variables as unitless. In Example #4, we present a dimensionally realistic simulation. The top panel of Figure 6

demonstrates that the variance of the ensemble of $\mathbf{Y}^N$ grows as certain ensemble members become large (in absolute value) over time.

Each ensemble member in the top panel of Figure 6 is colored to improve the visibility of the individual model trajectories. Each model is colored based on its sorted position at the end of the simulation ($t = N\Delta t = 400$), with red colors indicating large negative values of Y^N, blue colors representing large positive values of Y^N, and green colors representing near zero values of Y^N. Notice, that the color gradation appears relatively early in the simulation, e.g., ($t = N\Delta t > \sim 25$). In other words, the ranking of the ensemble members of $\mathbf{Y}^N$ develops relatively quickly, and members maintain their rank throughout the course of the simulation. The bottom panel of Figure 6 shows the simulated ensemble variance, $\mathrm{var}\left(\mathbf{Y}^n\right)$, based on the trajectories of Y shown in the top panel, compared to the theoretical variance growth rate in Equation 49. Overall, the simulated ensemble variance agrees with the theoretical result, with only slight deviations from the trivial bias of computer-generated, normally distributed random numbers within a finite sample size.

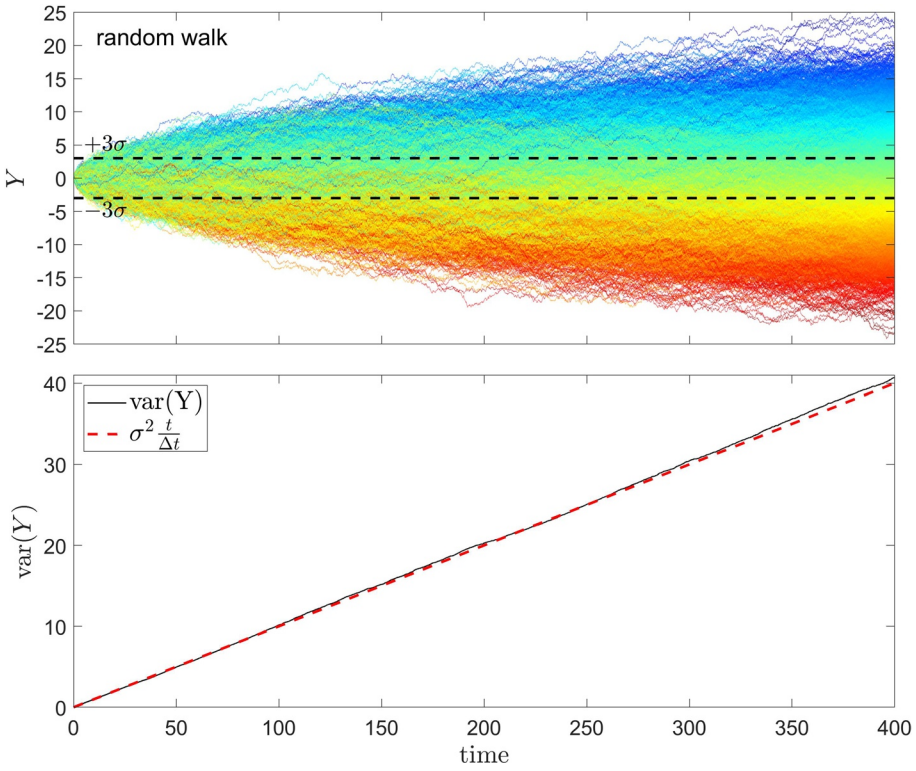

Figure 6. An ensemble simulation of the random walk governed by Equation 40 with $N_{\mathrm{ens}} = 10{,}000$, $\sigma = 0.1$, and $\Delta t = 0.1$. The top panel shows the model trajectories of each member of the ensemble, which is colored based on its sorted position at the end of the simulation ($t = N\Delta t = 400$), with red colors indicating large negative values of Y^N, blue colors representing large positive values of Y^N, and green colors representing near zero values of Y^N. The bottom panel shows the simulated ensemble variance (calculated from the trajectories of Y shown in the top panel) compared to the theoretical variance growth rate of $\sigma^2 t \,/\, \Delta t$.

Example #2: Damped random walk ensemble

The second model we consider is a damped random walk, which is given by

$$\frac{dY}{dt} = \frac{\varepsilon}{\Delta t} - \frac{Y}{\Delta T} \tag{50}$$

The governing Equation 50 includes additive noise as in Equation 39 plus an additional term (i.e., the second term on the right-hand side) that represents damping. Recall, that the simplest ordinary differential equation exhibiting this form of damping is $\frac{dY}{dt} = -\lambda Y$ for which the solution is an exponential decay, $Y = Y_0 \exp(-\lambda t)$. The simplified, linear damping term in Equation 50 is analogous to that of the modified Yates et al. (2009) model presented here in Equations 5 and 8, which decreases the tendency for additional erosion or accretion while the beach is currently in an eroded or accreted state, respectively. The damping term in Equation 50 contains a parameter, ΔT, which represents the time scale of damping. Small or large values of ΔT correspond to rapidly or slowly damped behavior, respectively.

The numerical model governing the evolution of Equation 50 becomes:

$$\frac{\mathbf{Y}^{n+1} - \mathbf{Y}^n}{\Delta t} = \frac{\boldsymbol{\varepsilon}^n}{\Delta t} - \frac{\mathbf{Y}^n}{\Delta T}$$

$$\mathbf{Y}^{n+1} = \mathbf{Y}^n + \boldsymbol{\varepsilon}^n - \frac{\Delta t}{\Delta T}\mathbf{Y}^n$$

$$\mathbf{Y}^{n+1} = \left(1 - \frac{\Delta t}{\Delta T}\right)\mathbf{Y}^n + \boldsymbol{\varepsilon}^n$$

$$\mathbf{Y}^{n+1} = \lambda \mathbf{Y}^n + \boldsymbol{\varepsilon}^n \tag{51}$$

where $\lambda = 1 - \Delta t / \Delta T$, which, in general, should be less than one as the model time step generally must be chosen to be less than the damping time scale, $\Delta t < \Delta T$. The alternative ($\Delta t > \Delta T$) will result in numerical instability. Thus, $\lambda < 1$ and we will see a muted response in the ensemble trajectories of Equation 51 in comparison with Equation 36.

Evaluating Equation 51 over the first few time steps gives

$$\mathbf{Y}^1 = \lambda \mathbf{Y}^0 + \boldsymbol{\varepsilon}^0$$

$$\mathbf{Y}^2 = \lambda \mathbf{Y}^1 + \boldsymbol{\varepsilon}^1 = \lambda\left(\lambda \mathbf{Y}^0 + \boldsymbol{\varepsilon}^0\right) + \boldsymbol{\varepsilon}^1 = \lambda^2 \mathbf{Y}^0 + \lambda \boldsymbol{\varepsilon}^0 + \boldsymbol{\varepsilon}^1$$

$$\mathbf{Y}^3 = \lambda \mathbf{Y}^2 + \boldsymbol{\varepsilon}^2 = \lambda\left(\lambda^2 \mathbf{Y}^0 + \lambda \boldsymbol{\varepsilon}^0 + \boldsymbol{\varepsilon}^1\right) + \boldsymbol{\varepsilon}^2 = \lambda^3 \mathbf{Y}^0 + \lambda^2 \boldsymbol{\varepsilon}^0 + \lambda \boldsymbol{\varepsilon}^1 + \boldsymbol{\varepsilon}^2$$

....

$$\mathbf{Y}^N = \lambda^N \mathbf{Y}^0 + \lambda^{N-1} \boldsymbol{\varepsilon}^0 + \lambda^{N-2} \boldsymbol{\varepsilon}^1 + \lambda^{N-3} \boldsymbol{\varepsilon}^2 + \ldots + \lambda^2 \boldsymbol{\varepsilon}^{N-3} + \lambda \boldsymbol{\varepsilon}^{N-2} + \boldsymbol{\varepsilon}^{N-1} \tag{52}$$

$$\mathbf{Y}^N = \lambda^N \mathbf{Y}^0 + \sum_{i=0}^{N-1} \lambda^i \boldsymbol{\varepsilon}^{N-1-i} \tag{53}$$

Thus, since $\lambda < 1$, then even though the noise becomes accumulated over time in Equation 52, we see that terms representing the older values of the additive noise and the initial conditions become increasingly damped by higher powers of λ. Note, that when $\lambda < 1$, then $\lambda^p \to 0$ as $p \to \infty$. Thus, the final state Y is primarily determined by some combination of 'recent' perturbations. The memory the past state of Y and past perturbations to it, $\boldsymbol{\varepsilon}$, become lost after a certain time (which depends on the degree of damping). In Equation 52, the initial conditions in play only a transient role, because after many time steps $\lambda^N \to 0$ and therefore the initial conditions are not remembered the final state. In other words, the 'memory' or influence of the initial condition decays exponentially with time or with the number of time steps, N.

We can estimate the number of time steps required for the initial conditions to be 'forgotten' by the following analysis. If we assume that the initial conditions become negligible in Equation 52 when $\lambda^N = 0.01$, then we can rearrange this equation to calculate the number of time steps N before the memory of the initial conditions are lost, which is given by

$$\begin{aligned}\lambda^N &= 0.01\\ N\log_{10}(\lambda) &= \log_{10}(0.01)\\ N\log_{10}(\lambda) &= -2\\ N &= \frac{-2}{\log_{10}(\lambda)}\end{aligned}$$

For a typical value of damping of $\lambda = 1 - \frac{\Delta t}{\Delta T} = 1 - \frac{1\,\text{day}}{21\,\text{days}} \approx 0.95$, resulting in $\log_{10}(\lambda) \approx -0.02$, then the memory time scale is $N \approx 100$ time steps.

This example illustrates the concept of "beach memory" that has been discussed in the literature (Jara et al. 2015, 2018; Reeve et al., 2014; Turki et al. 2012, 2013). Here, we define beach memory as the degree to which the current shoreline state "remembers" or "forgets" its past state and antecedent wave conditions. According to Equations 50 and 52, it is evident that the process that is directly responsible for limiting "beach memory" is some form of damping to the system, like that contained in the Yates et al. (2009) model.

We can calculate the variance of the ensemble at time step N, that is, $\text{var}\left(\mathbf{Y}^N\right)$, by taking the variance of Equation 52

$$\begin{aligned}\text{var}\left(\mathbf{Y}^N\right) &= \text{var}\left(\lambda^N\mathbf{Y}^0 + \sum_{i=0}^{N-1}\lambda^i\boldsymbol{\varepsilon}^{N-1-i}\right)\\ &= \text{var}\left(\lambda^N\mathbf{Y}^0\right) + \text{var}\left(\sum_{i=0}^{N-1}\lambda^i\boldsymbol{\varepsilon}^{N-1-i}\right)\end{aligned} \tag{54}$$

where we have applied the assumption that the initial conditions are uncorrelated with the additive noise. Further, we assume that the realizations of (white) noise are uncorrelated, and thus Equation 54 becomes:

$$\text{var}\left(\mathbf{Y}^N\right) = \left(\lambda^N\right)^2\text{var}\left(\mathbf{Y}^0\right) + \sum_{i=0}^{N-1}\left(\lambda^i\right)^2\text{var}\left(\boldsymbol{\varepsilon}^{N-1-i}\right)$$

where we have applied the property that $\text{var}(\lambda\boldsymbol{\varepsilon}) = \lambda^2\,\text{var}(\boldsymbol{\varepsilon})$. Next, applying $\text{var}\left(\boldsymbol{\varepsilon}^n\right) = \sigma^2$ and rearranging the exponents gives

$$\begin{aligned}\text{var}\left(\mathbf{Y}^N\right) &= \left(\lambda^2\right)^N\text{var}\left(\mathbf{Y}^0\right) + \sum_{i=0}^{N-1}\left(\lambda^2\right)^i\sigma^2\\ &= \left(\lambda^2\right)^N\text{var}\left(\mathbf{Y}^0\right) + \sigma^2\left(\sum_{i=0}^{N-1}\left(\lambda^2\right)^i\right)\end{aligned} \tag{55}$$

Note that because σ is a constant, it can be taken outside of the summation.

Substituting $\frac{1}{\alpha} = \lambda^2$ in Equation 55 gives,

$$\text{var}\left(\mathbf{Y}^N\right) = \left(\frac{1}{\alpha}\right)^N\text{var}\left(\mathbf{Y}^0\right) + \sigma^2\left(\sum_{i=0}^{N-1}\frac{1}{\alpha^i}\right) \tag{56}$$

In this case, since $\alpha = \frac{1}{\lambda^2}$ and $\lambda < 1$, then $\alpha > 1$. For simplicity, we assume that there is a value $M < N$ that is sufficiently large so that $\left(\frac{1}{\alpha}\right)^M \approx 0$ and Equation 56 becomes

$$\mathrm{var}\left(\mathbf{Y}^N\right) \approx \left(\sum_{i=0}^{\infty} \frac{1}{\alpha^i}\right)\sigma^2 \tag{57}$$

which indicates that the 'memory' of the initial conditions has become lost. We can further modify Equation 57 by using an identity which says that the sum of reciprocal powers of any number $\alpha > 1$ produces a convergent series solution given by

$$\sum_{i=0}^{\infty} \frac{1}{\alpha^i} = \frac{\alpha}{\alpha - 1}. \tag{58}$$

Thus, after substituting Equation 58, then Equation 57 can be written as

$$\mathrm{var}\left(\mathbf{Y}^N\right) \approx \left(\frac{\alpha}{\alpha - 1}\right)\sigma^2 = \sigma^2_{\max} \tag{59}$$

where $\sigma^2_{\max}$ represents the approximate maximum variance of the model ensemble. Unlike the behavior of the variance described in Equation 49 which grows over time, the behavior of the variance of the damped random walk, as described in Equation 59, is approximately bounded by $\sigma^2_{\max}$. The maximum variance is determined from a balance between the rate at which noise/variance is injected into the solution, e.g., σ, and the rate at which variance is removed through damping, e.g., via $\lambda < 1$ on Equation 51 or via the coefficient $\frac{\alpha}{\alpha - 1}$ on Equation 59. This result is consistent with our intuition: large perturbations causing the current state to differ significantly from the background state will be suppressed by damping much more rapidly than small perturbations according to Equation 50. Consequently, all of the members of the ensemble will become driven to fall within an *equilibrium range*, which is approximately given by $\pm 3\sigma_{\max}$. Here, $\pm 3\sigma_{\max}$ does not represent absolute bounds on the modeled position Y. However, based on the Gaussian statistics applied here, we expect that ~99.7% of modeled position will fall within this equilibrium range (for the all of the following examples). Instantaneous deviations from this equilibrium range, while possible, will be quickly suppressed due to imbalance of damping relative to perturbations from the random walk.

Figure 7 illustrates an ensemble simulation of the damped random walk governed by Equation 50 with $N_{\mathrm{ens}} = 10{,}000$, $\sigma = 0.1$, $\Delta t = 0.1$, and $\Delta T = 200\Delta t$. The top panel of Figure 7 demonstrates that the spread of the ensemble $\mathbf{Y}^n$ initially grows over time, but that eventually the ensemble settles into an equilibrium range given by $\pm 3\sigma_{\max}$. By the time that $t >\sim 40$, we see that the ensemble variance is very close to the theoretical upper limit. Each ensemble member in the top panel of Figure 7 is colored similarly to Figure 6, where the colors of individual simulations are based on their sorted position at the end of the simulation ($t = N\Delta t = 400$), with red colors indicating large negative values of Y^N, blue colors representing large positive values of Y^N, and green colors representing near zero values of Y^N. Notice that the color gradation does not appear until relatively late in the simulation, in contrast to Figure 6. This indicates that the ensemble members of $\mathbf{Y}^N$ can readily change their rank throughout the course of the simulation because any errant model trajectories are rapidly suppressed via damping. The bottom panel of Figure 7 shows the simulated ensemble variance, $\mathrm{var}\left(\mathbf{Y}^n\right)$, computed from the trajectories of Y shown in the top panel, compared to the theoretical variance growth rate in Equation 49 and the theoretical maximum variance in Equation 59. Overall, the simulated ensemble variance growth rates and limits agree with the theoretical results, with only slight deviations due to computer-generated biases in the random number generator.

Example #3: forced, damped random walk ensemble

The third model, which combines additive noise, damping, and forcing, is given by

$$\frac{dY}{dt} = \frac{\varepsilon}{\Delta t} - \frac{Y}{\Delta T} + \frac{f(t)}{\Delta T_f} \tag{60}$$

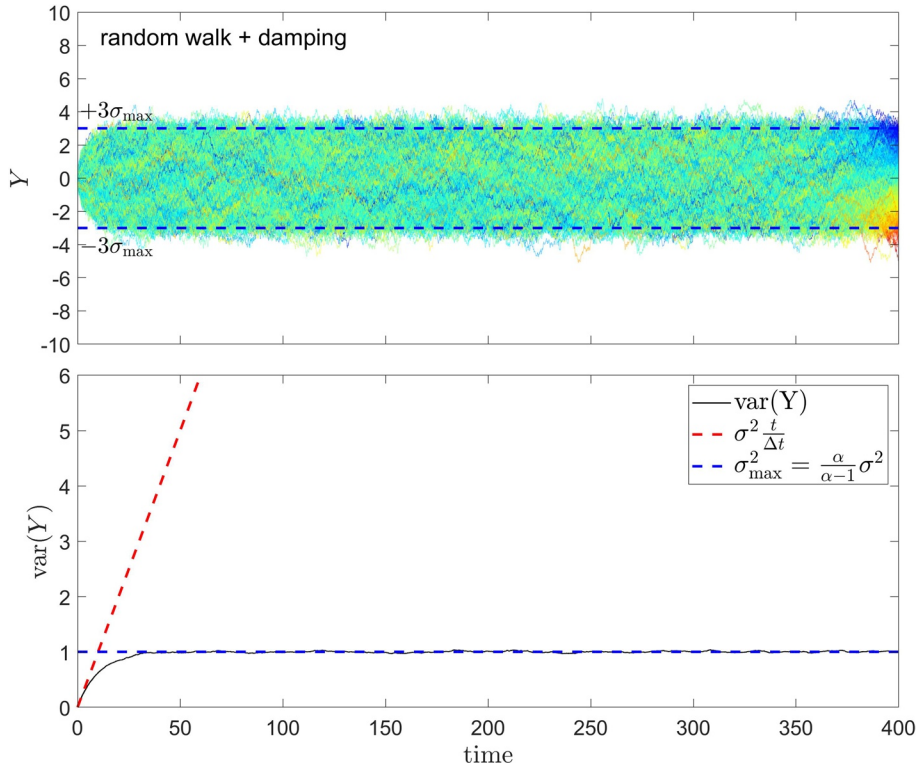

Figure 7. An ensemble simulation of the damped random walk governed by Equation 50 with $N_{ens} = 10{,}000$, $\sigma = 0.1$, $\Delta t = 0.1$, and $\Delta T = 200\Delta t$. The top panel shows that the model trajectories of each member of the ensemble, which are colored similarly to Figure 6, are roughly bounded by $\pm 3\sigma_{max}$. The bottom panel shows the simulated ensemble variance, computed from the trajectories of Y shown in the top panel, compared to the theoretical variance growth rate of $\sigma^2 t / \Delta t$ in the absence of damping, and the theoretical upper limit to the variance based on Equation 59. Although the variance grows initially at the expected rate, it quickly becomes bounded at the theoretical value due to the damping in the model.

where $f(t)$ is a time series of forcing conditions and ΔT_f is the time scale associated with the adjustment of the solution Y to the forcing. In Equation 60, a large value of ΔT_f means a slow, muted response to the forcing conditions and a small value of ΔT_f means a rapid, direct response to the forcing conditions.

A numerical model governing the evolution equation of Equation 60 is given by

$$\frac{\mathbf{Y}^{n+1} - \mathbf{Y}^n}{\Delta t} = \frac{\boldsymbol{\varepsilon}^n}{\Delta t} - \frac{\mathbf{Y}^n}{\Delta T} + \frac{\mathbf{f}^n}{\Delta T_f}$$

$$\mathbf{Y}^{n+1} = \mathbf{Y}^n + \boldsymbol{\varepsilon}^n - \frac{\Delta t}{\Delta T}\mathbf{Y}^n + \frac{\Delta t}{\Delta T_f}\mathbf{f}^n$$

$$\mathbf{Y}^{n+1} = \left(1 - \frac{\Delta t}{\Delta T}\right)\mathbf{Y}^n + \boldsymbol{\varepsilon}^n + \frac{\Delta t}{\Delta T_f}\mathbf{f}^n$$

$$\mathbf{Y}^{n+1} = \lambda \mathbf{Y}^n + \boldsymbol{\varepsilon}^n + \frac{\Delta t}{\Delta T_f}\mathbf{f}^n \tag{61}$$

Evaluating Equation 61 over the first few time steps gives

$$
\begin{aligned}
\mathbf{Y}^1 &= \lambda\mathbf{Y}^0 + \boldsymbol{\varepsilon}^0 + \frac{\Delta t}{\Delta T_f}\mathbf{f}^0 \\
\mathbf{Y}^2 &= \lambda\mathbf{Y}^1 + \boldsymbol{\varepsilon}^1 + \frac{\Delta t}{\Delta T_f}\mathbf{f}^1 = \lambda\left(\lambda\mathbf{Y}^0 + \boldsymbol{\varepsilon}^0 + \frac{\Delta t}{\Delta T_f}\mathbf{f}^0\right) + \boldsymbol{\varepsilon}^1 + \frac{\Delta t}{\Delta T_f}\mathbf{f}^1 \\
&= \lambda^2\mathbf{Y}^0 + \lambda\left(\boldsymbol{\varepsilon}^0 + \frac{\Delta t}{\Delta T_f}\mathbf{f}^0\right) + \boldsymbol{\varepsilon}^1 + \frac{\Delta t}{\Delta T_f}\mathbf{f}^1 \\
\mathbf{Y}^3 &= \lambda\mathbf{Y}^2 + \boldsymbol{\varepsilon}^2 + \frac{\Delta t}{\Delta T_f}\mathbf{f}^2 = \lambda\left(\lambda^2\mathbf{Y}^0 + \lambda\left(\boldsymbol{\varepsilon}^0 + \frac{\Delta t}{\Delta T_f}\mathbf{f}^0\right) + \boldsymbol{\varepsilon}^1 + \frac{\Delta t}{\Delta T_f}\mathbf{f}^1\right) + \boldsymbol{\varepsilon}^2 + \frac{\Delta t}{\Delta T_f}\mathbf{f}^2 \\
&= \lambda^3\mathbf{Y}^0 + \lambda^2\left(\boldsymbol{\varepsilon}^0 + \frac{\Delta t}{\Delta T_f}\mathbf{f}^0\right) + \lambda\left(\boldsymbol{\varepsilon}^1 + \frac{\Delta t}{\Delta T_f}\mathbf{f}^1\right) + \boldsymbol{\varepsilon}^2 + \frac{\Delta t}{\Delta T_f}\mathbf{f}^2 \\
&\cdots \\
\mathbf{Y}^N &= \lambda^N\mathbf{Y}^0 + \lambda^{N-1}(\boldsymbol{\varepsilon}^0 + \frac{\Delta t}{\Delta T_f}\mathbf{f}^0) + \cdots + \lambda(\boldsymbol{\varepsilon}^{N-2} + \frac{\Delta t}{\Delta T_f}\mathbf{f}^{N-2}) + \boldsymbol{\varepsilon}^{N-1} + \frac{\Delta t}{\Delta T_f}\mathbf{f}^{N-1} \qquad (62)
\end{aligned}
$$

$$
\mathbf{Y}^N = \lambda^N\mathbf{Y}^0 + \sum_{i=0}^{N-1}\lambda^i\left(\boldsymbol{\varepsilon}^{N-1-i} + \frac{\Delta t}{\Delta T_f}\mathbf{f}^{N-1-i}\right) \qquad (63)
$$

The only difference between Equations 52 and 53 and Equations 62 and 63 is the presence of the additional forcing terms.

Taking the variance of Equation 63 gives:

$$
\mathrm{var}\left(\mathbf{Y}^N\right) = \mathrm{var}\left(\lambda^N\mathbf{Y}^0 + \sum_{i=0}^{N-1}\lambda^i\left(\boldsymbol{\varepsilon}^{N-1-i} + \frac{\Delta t}{\Delta T_f}\mathbf{f}^{N-1-i}\right)\right) \qquad (64)
$$

Assuming that none of the variables on the RHS of Equation 64 are correlated with each other gives

$$
\mathrm{var}\left(\mathbf{Y}^N\right) = \mathrm{var}\left(\lambda^N\mathbf{Y}^0\right) + \mathrm{var}\left(\sum_{i=0}^{N-1}\lambda^i\boldsymbol{\varepsilon}^{N-1-i}\right) + \left(\frac{\Delta t}{\Delta T_f}\right)^2\mathrm{var}\left(\sum_{i=0}^{N-1}\lambda^i\mathbf{f}^{N-1-i}\right) \qquad (65)
$$

Assuming that the (white) noise is uncorrelated with itself, then Equation 65 becomes

$$
\begin{aligned}
\mathrm{var}\left(\mathbf{Y}^N\right) &= \left(\lambda^N\right)^2\mathrm{var}\left(\mathbf{Y}^0\right) + \sum_{i=0}^{N-1}\left(\lambda^i\right)^2\mathrm{var}\left(\varepsilon^{N-1-i}\right) + \left(\frac{\Delta t}{\Delta T_f}\right)^2\mathrm{var}\left(\sum_{i=0}^{N-1}\lambda^i\mathbf{f}^{N-1-i}\right) \\
&= \left(\lambda^2\right)^N\mathrm{var}\left(\mathbf{Y}^0\right) + \sum_{i=0}^{N-1}\left(\lambda^2\right)^i\sigma^2 + \left(\frac{\Delta t}{\Delta T_f}\right)^2\mathrm{var}\left(\sum_{i=0}^{N-1}\lambda^i\mathbf{f}^{N-1-i}\right) \\
&= \left(\lambda^2\right)^N\mathrm{var}\left(\mathbf{Y}^0\right) + \sigma^2\sum_{i=0}^{N-1}\left(\lambda^2\right)^i + \left(\frac{\Delta t}{\Delta T_f}\right)^2\mathrm{var}\left(\sum_{i=0}^{N-1}\lambda^i\mathbf{f}^{N-1-i}\right) \\
&= \left(\frac{1}{\alpha}\right)^N\mathrm{var}\left(\mathbf{Y}^0\right) + \sigma^2\sum_{i=0}^{N-1}\left(\frac{1}{\alpha}\right)^i + \left(\frac{\Delta t}{\Delta T_f}\right)^2\mathrm{var}\left(\sum_{i=0}^{N-1}\lambda^i\mathbf{f}^{N-1-i}\right)
\end{aligned} \qquad (66)
$$

After assuming that $1 / \alpha^N \to 0$ (for a large value of N), Equation 66 becomes

$$
\mathrm{var}\left(\mathbf{Y}^N\right) \approx \sigma^2\sum_{i=0}^{N-1}\left(\frac{1}{\alpha}\right)^i + \left(\frac{\Delta t}{\Delta T_f}\right)^2\mathrm{var}\left(\sum_{i=0}^{N-1}\lambda^i\mathbf{f}^{N-1-i}\right) \qquad (67)
$$

If the forcing term is uncorrelated with itself, then Equation 67 becomes

$$\begin{aligned}\mathrm{var}\left(\mathbf{Y}^N\right) &\approx \sigma^2\sum_{i=0}^{N-1}\left(\frac{1}{\alpha}\right)^i + \left(\frac{\Delta t}{\Delta T_f}\right)^2\sum_{i=0}^{N-1}\left(\lambda^i\right)^2\mathrm{var}\left(\mathbf{f}^{N-1-i}\right)\\ &\approx \sigma^2\sum_{i=0}^{N-1}\left(\frac{1}{\alpha}\right)^i + \left(\frac{\Delta t}{\Delta T_f}\right)^2\sum_{i=0}^{N-1}\left(\frac{1}{\alpha}\right)^i\mathrm{var}\left(\mathbf{f}^{N-1-i}\right)\end{aligned} \tag{68}$$

We will return to this assumption later and address the case where the forcing is correlated with itself in the following example.

If the forcing term is also drawn from a normal distribution, $f \sim \mathcal{N}\left(0,\sigma_f^2\right)$ then its variance is given by

$$\mathrm{var}\left(\mathbf{f}^n\right) = \sigma_f^2, \tag{69}$$

then Equation 68 becomes

$$\begin{aligned}\mathrm{var}\left(\mathbf{Y}^N\right) &\approx \sigma^2\sum_{i=0}^{N-1}\left(\frac{1}{\alpha}\right)^i + \left(\frac{\Delta t}{\Delta T_f}\right)^2\sum_{i=0}^{N-1}\left(\frac{1}{\alpha}\right)^i\sigma_f^2\\ &\approx \sigma^2\sum_{i=0}^{N-1}\left(\frac{1}{\alpha}\right)^i + \left(\frac{\Delta t}{\Delta T_f}\right)^2\sigma_f^2\sum_{i=0}^{N-1}\left(\frac{1}{\alpha}\right)^i\\ &\approx \sum_{i=0}^{N-1}\left(\frac{1}{\alpha}\right)^i\left[\sigma^2 + \left(\frac{\Delta t}{\Delta T_f}\right)^2\sigma_f^2\right]\end{aligned} \tag{70}$$

Applying the converging series solution in Equation 58, Equation 70 becomes

$$\mathrm{var}\left(\mathbf{Y}^N\right) \approx \left(\frac{\alpha}{\alpha-1}\right)\left[\underbrace{\sigma^2}_{\substack{\text{variance}\\ \text{contribution}\\ \text{from}\\ \text{additive noise}}} + \underbrace{\left(\frac{\Delta t}{\Delta T_f}\right)^2\sigma_f^2}_{\substack{\text{variance}\\ \text{contribution}\\ \text{from forcing}}}\right] = \sigma_{f,\max}^2 \tag{71}$$

without the presence of the damping term, then Equation 71 becomes

$$\mathrm{var}\left(\mathbf{Y}^N\right) \approx N\left[\sigma^2 + \left(\frac{\Delta t}{\Delta T_f}\right)^2\sigma_f^2\right] = \left[\sigma^2 + \left(\frac{\Delta t}{\Delta T_f}\right)^2\sigma_f^2\right]\frac{t}{\Delta t} \tag{72}$$

which again represents a linear growth in the variance with time (or with the number of time steps), albeit at a larger growth rate due to the presence of the additional variance generated by the forcing.

Figure 8 illustrates an ensemble simulation of the forced, damped random walk governed by Equation 60 with $N_{\mathrm{ens}} = 10{,}000$, $\sigma = 0.1$, $\Delta t = 0.1$, $\Delta T = 200\Delta t$, and $\Delta T_f = 2\Delta t$. The forcing f function is drawn from a normally distributed random number generator with zero mean and standard deviation $\sigma_f = 0.3$. The top panel of Figure 8 demonstrates that the spread of the ensemble of $\mathbf{Y}^N$ initially grows over time, but that eventually the ensemble settles into an equilibrium range given by $\pm 3\sigma_{f,\max}$. By the time that $t >\sim 40$, we see that the ensemble variance is very close to the theoretical upper limit. Each ensemble member in the top panel of Figure 8 is colored similarly to Figure 6, where the colors of individual simulations are based on their sorted position at the end of the simulation ($t = N\Delta t = 400$), as in the previous simulations. Notice, that the color gradation does not appear until relatively late in the simulation, in contrast to Figure 6. Like in Figure 7, the ensemble members of $\mathbf{Y}^N$ can readily change their position and rank throughout the course

of the simulation. The bottom panel of Figure 8 shows the simulated ensemble variance, $\mathrm{var}\left(\mathbf{Y}^N\right)$, based on the trajectories of Y shown in the top panel, compared to the theoretical variance growth rate in Equation 72 and the theoretical maximum variance in Equation 71. Overall, the simulated ensemble variance growth rates and limits agree with the theoretical results.

Figure 9 illustrates an identical simulation to Figure 9, except with uniform forcing, meaning that a single realization of the random forcing function is applied to each member of ensemble. Consequently, all of the members of the ensemble experience a consistent fluctuation throughout the course of the simulation, as shown in the top panel of Figure 10. Although the trajectories of the model ensembles are roughly bounded by $\pm 3\sigma_{f,\max}$ in the top panel of Figure 10, the variance of the ensemble is roughly bounded by $\sigma^2_{\max}$, based on Equation 59. The uniformly forced simulation *does not* include the additional variance due to the forcing as in Equation 71. Because there is no variance among the (uniform) model forcing throughout the ensemble, then the variance of the ensemble is only driven by the variance generated from the combined noise and damping (as in *Example #2*). This example demonstrates that the single realization approach does not capture any intrinsic uncertainty in the forcing.

Figure 10 illustrates an identical simulation to Figure 10, except that the uniform forcing is applied across for each member of the ensemble for $t < 200$ and then transitions to a random, ensemble (as in Figure 9) for $t \geq 200$. The transition from a uniform forcing to an ensemble forcing is meant to represent the transition from a hindcast (with known forcing conditions) to an ensemble forecast (with unknown future forcing conditions). Hence, the variance of the ensemble forecast with stochastic forcing will be inherently larger than the variance of the hindcast. This is evident in the top panel of Figure 10, where the spread of

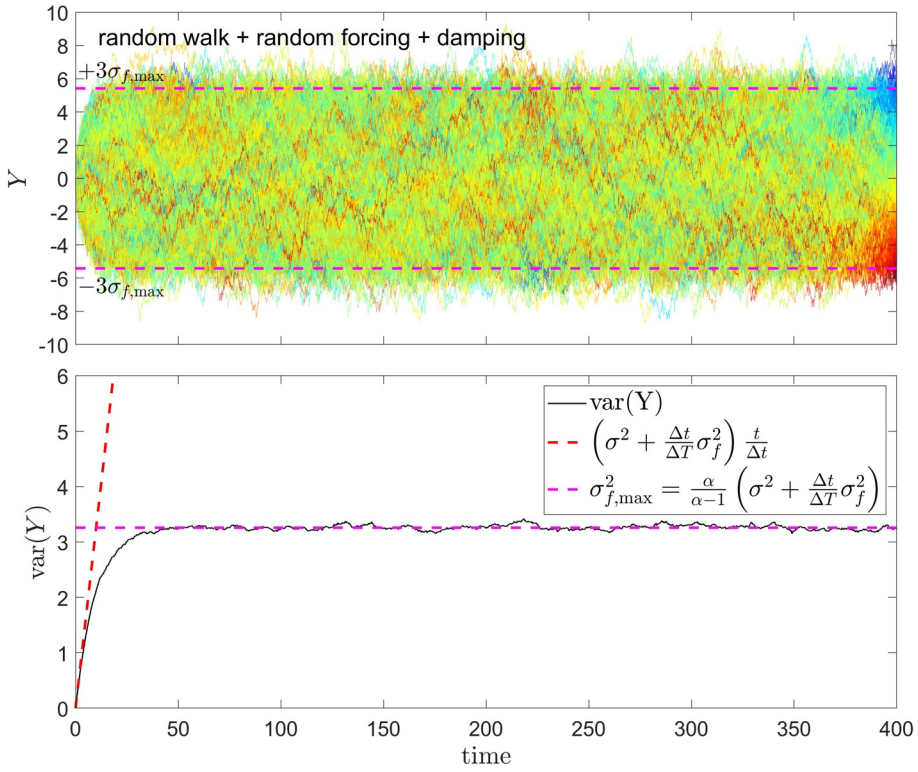

Figure 8. An ensemble simulation of the forced, damped random walk governed by Equation 60 with $N_{\mathrm{ens}} = 10{,}000$, $\sigma = 0.1$, $\Delta t = 0.1$, $\Delta T = 200\Delta t$, and $\Delta T_f = 2\Delta t$. The forcing f, in this example, is drawn from a normally distributed random number generator with zero mean and standard deviation $\sigma_f = 0.3$. The top panel shows that the model trajectories of each member of the ensemble, which are colored similarly to Figures 6 and 7, are roughly bounded by $\pm 3\sigma_{f,\max}$. The bottom panel shows the simulated ensemble variance, based on the trajectories of Y shown in the top panel, compared to the theoretical variance growth rate given in Equation 72 in the absence of damping, and the theoretical upper limit to the variance based on Equation 71.

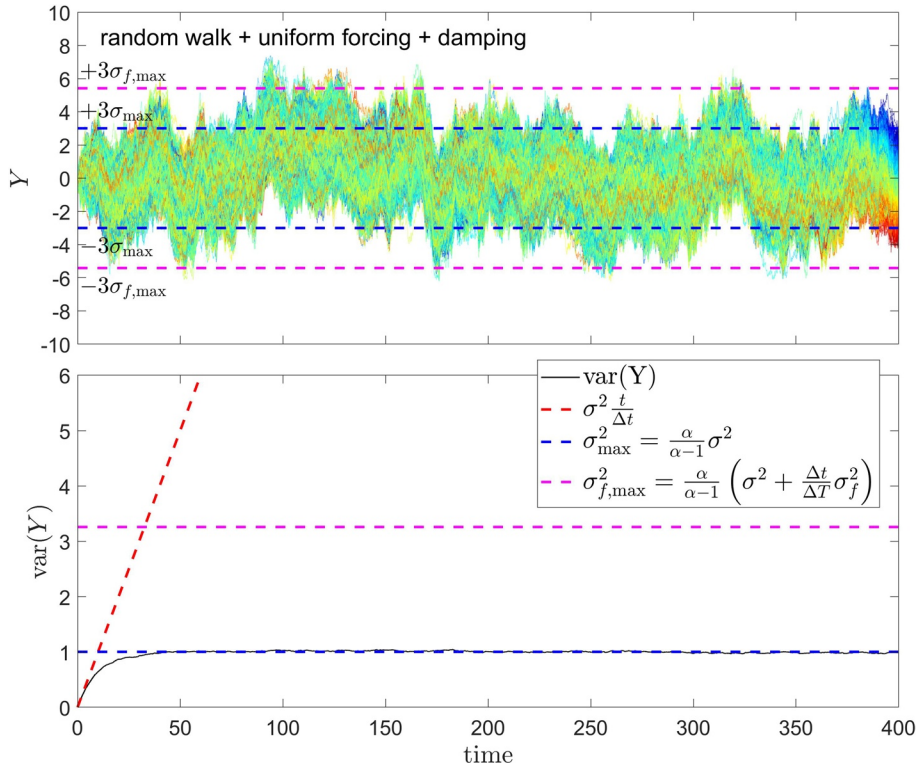

Figure 9. An ensemble simulation of a uniformly forced, damped random walk governed by Equation 60 with $N_{ens} = 10{,}000$, $\sigma = 0.1$, $\Delta t = 0.1$, $\Delta T = 200\Delta t$, and $\Delta T_f = 2\Delta t$. The forcing f, in this example, is drawn from a single realization of a normally distributed random number generator with zero mean and standard deviation $\sigma_f = 0.3$, which is applied uniformly across for each member of the ensemble. The top panel shows that the model trajectories of each member of the ensemble, which are colored similarly to Figures 6 and 7, are roughly bounded by $\pm 3\sigma_{f,\max}$. The bottom panel shows the simulated ensemble variance, computed from the trajectories of Y shown in the top panel, compared to the theoretical variance growth rate given in Equation 49 in the absence of damping, and the theoretical upper limit to the variance, $\sigma^2_{\max}$, based on Equation 59. Note that the upper limit of the variance, $\sigma^2_{f,\max}$, given in Equation 71, pertains to a randomly forced ensemble. When all of the models are uniformly forced, then the variance contributed by the forcing is identically zero. Hence, the modeled variance is created only by the combination of noise and damping (i.e., $\sigma^2_{\max}$).

the model trajectories becomes much larger as the model transitions from a uniformly forced hindcast to an ensemble forecast at $t = 200$. Once again, the bottom panel of Figure 10 shows the simulated ensemble variance based on the trajectories of Y shown in the top panel. For $t < 200$, the variance of the ensemble initially grows at the theoretical variance growth rate given in Equation 49 then stabilizes at the theoretical upper bound of $\sigma^2_{\max}$, based on Equation 59. After the start of the random forcing at $t = 200$, the variance of the model grows at the theoretical variance growth rate given in Equation 72 and then stabilizes at the theoretical upper bound of $\sigma^2_{f,\max}$, based on Equation 71. Overall, Figure 10 demonstrates the fundamental role that both uniform and ensemble forcing conditions play in the variance of the model.

Example #4: Idealized shoreline change ensemble based on Yates et al. (2009)

In our final example, we return to the modified Yates et al. (2009) model in Equations 5–7 which is given by

$$\frac{dY}{dt} = \frac{1}{\Delta T}\left(\frac{H_s}{\hat{H}_s}\right)\left(-\Delta Y \frac{H_s^2 - \hat{H}_s^2}{\hat{H}_s^2} - Y\right) + \frac{\varepsilon}{\Delta t} \tag{73}$$

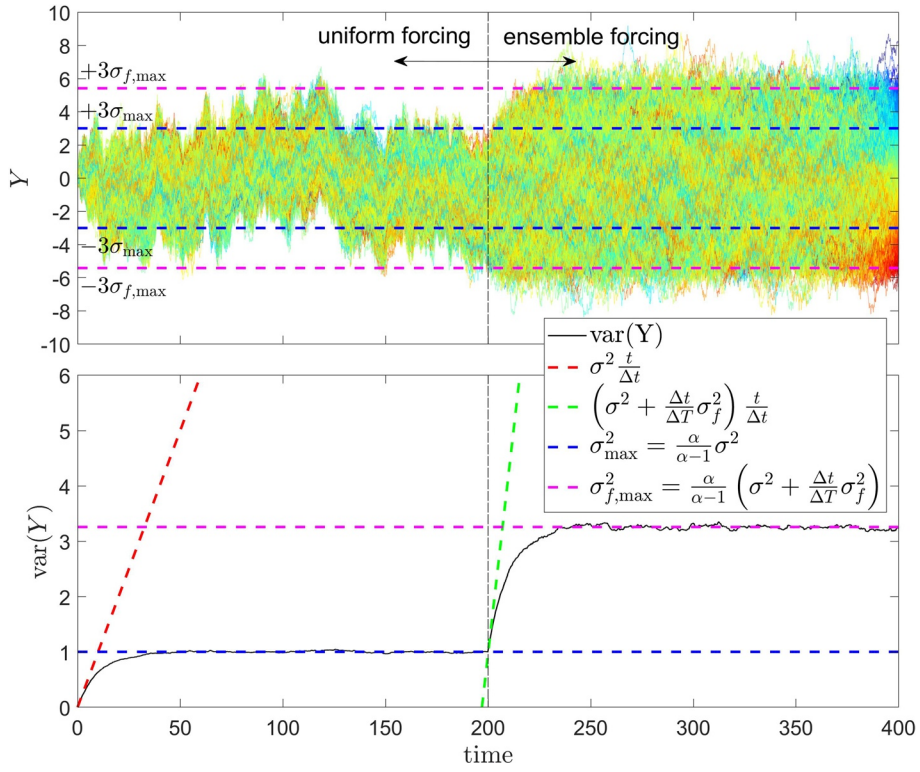

Figure 10. An ensemble simulation of the forced, damped random walk governed by Equation 60 with $N_{\text{ens}} = 10{,}000$, $\sigma = 0.1$, $\Delta t = 0.1$, $\Delta T = 200\Delta t$, and $\Delta T_f = 2\Delta t$. The forcing f, in this example, is drawn from a normally distributed random number generator with zero mean and variance $\sigma_f = 0.3$. The forcing is applied uniformly across for each member of the ensemble for $t < 200$ and is random for each member of the ensemble for $t \geq 200$. The top panel shows that the model trajectories of each member of the ensemble, which are colored similarly to Figure 6 and Figure 7, are roughly bounded by $\pm 3\sigma_{f,\max}$. The bottom panel shows the simulated ensemble variance, computed from the trajectories of Y shown in the top panel, compared to the theoretical variance growth rate given in Equation 49 or 72 in the absence of damping, and the theoretical upper limit to the variance, $\sigma^2_{\max}$, based on Equation 59 and $\sigma^2_{F,\max}$, based on Equation 71. Note that the overall variance of the model grows rapidly at the onset of the random forcing at $t = 35$ and then stabilizes at the theoretical upper bound of $\sigma^2_{f,\max}$, based on Equation 71.

where additive noise has also been included in the model.

Distributing the time-scale parameter into the forcing and damping terms in Equation 73 results in

$$\frac{dY}{dt} = \underbrace{-\frac{1}{\Delta T}\left(\frac{H_s}{\hat{H}_s}\right)Y}_{\text{damping}} \underbrace{-\frac{\Delta Y}{\Delta T}\left(\frac{H_s}{\hat{H}_s}\frac{H_s^2 - \hat{H}_s^2}{\hat{H}_s^2}\right)}_{\text{forcing}} + \underbrace{\frac{\varepsilon}{\Delta t}}_{\text{additive noise}} \tag{74}$$

where the three terms on the right-hand side of Equation 74 represent damping, forcing, and additive noise, respectively.

The ensemble model equation based on Equation 74 is given by

$$\frac{\mathbf{Y}^{n+1} - \mathbf{Y}^n}{\Delta t} = -\frac{1}{\Delta T}\left(\frac{\mathbf{H}_s}{\hat{H}_s}\right)\mathbf{Y}^n - \frac{\Delta \mathbf{Y}}{\Delta T}\frac{\mathbf{H}_s}{\hat{H}_s}\frac{H_s^2 - \hat{H}_s^2}{\hat{H}_s^2} + \frac{\boldsymbol{\varepsilon}^n}{\Delta t}$$

$$\mathbf{Y}^{n+1} = \mathbf{Y}^n - \frac{\Delta t}{\Delta T}\frac{\mathbf{H}_s}{\hat{H}_s}\mathbf{Y}^n - \frac{\Delta t}{\Delta T}\Delta \mathbf{Y}\frac{\mathbf{H}_s}{\hat{H}_s}\frac{H_s^2 - \hat{H}_s^2}{\hat{H}_s^2} + \boldsymbol{\varepsilon}^n$$

$$\mathbf{Y}^{n+1} = \left(1 - \frac{\Delta t}{\Delta T}\frac{\mathbf{H}_s}{\hat{H}_s}\right)\mathbf{Y}^n + \frac{\Delta t}{\Delta T}\left(-\Delta \mathbf{Y}\frac{\mathbf{H}_s}{\hat{H}_s}\frac{H_s^2 - \hat{H}_s^2}{\hat{H}_s^2}\right) + \boldsymbol{\varepsilon}^n$$

$$\mathbf{Y}^{n+1} = \lambda \mathbf{Y}^{n} + \frac{\Delta t}{\Delta T}\mathbf{f}^{n} + \boldsymbol{\varepsilon}^{n} \tag{75}$$

which is similar to the governing equation of Example #3 (i.e., Equation 61), where $\lambda = 1 - \frac{\Delta t}{\Delta T}\frac{\mathbf{H}_s}{\hat{H}_s}$. Here the damping term, λ, is not constant with time. However, here we approximate λ as a constant $\lambda \approx 1 - f_{H_s}\frac{\Delta t}{\Delta T}$, where $f_{H_s} = \frac{\mathbf{H}_s}{\hat{H}_s}$ represents the time and ensemble average of the normalized wave height. In the example of Tairua beach, $f_{H_s} = \mathbf{H}_s \,/\, \hat{H}_s \approx 0.7$, where the best-fit, background wave height is found to be $\hat{H}_s = 1.22$ m.

The forcing term in 75 is given by

$$\mathbf{f} = -\Delta\mathbf{Y}\frac{\mathbf{H}_s}{\hat{H}_s}\frac{\mathbf{H}_s^2 - \hat{H}_s^2}{\hat{H}_s^2} \tag{76}$$

Evaluating Equation 75 over N time steps, like in Equation 63, gives

$$\mathbf{Y}^{N} = \lambda^{N}\mathbf{Y}^{0} + \sum_{i=0}^{N-1}\lambda^{i}\left(\boldsymbol{\varepsilon}^{N-1-i} + \frac{\Delta t}{\Delta T}\mathbf{f}^{N-1-i}\right) \tag{77}$$

Taking the variance of Equation 77 gives:

$$\mathrm{var}\left(\mathbf{Y}^{N}\right) = \mathrm{var}\left(\lambda^{N}\mathbf{Y}^{0} + \sum_{i=0}^{N-1}\lambda^{i}\left(\boldsymbol{\varepsilon}^{N-1-i} + \frac{\Delta t}{\Delta T}\mathbf{f}^{N-1-i}\right)\right) \tag{78}$$

Assuming that the noise is uncorrelated with the initial conditions, the forcing, and itself, Equation 78 becomes

$$\begin{aligned}
\mathrm{var}\left(\mathbf{Y}^{N}\right) &= \left(\lambda^{N}\right)^{2}\mathrm{var}\left(\mathbf{Y}^{0}\right) + \left(\sum_{i=0}^{N-1}\left(\lambda^{i}\right)^{2}\mathrm{var}\left(\boldsymbol{\varepsilon}^{N-1-i}\right)\right) + \left(\frac{\Delta t}{\Delta T}\right)^{2}\mathrm{var}\left(\sum_{i=0}^{N-1}\lambda^{i}\mathbf{f}^{N-1-i}\right) \\
&= \left(\lambda^{2}\right)^{N}\mathrm{var}\left(\mathbf{Y}^{0}\right) + \left(\sum_{i=0}^{N-1}\left(\lambda^{2}\right)^{i}\mathrm{var}\left(\boldsymbol{\varepsilon}^{N-1-i}\right)\right) + \left(\frac{\Delta t}{\Delta T}\right)^{2}\mathrm{var}\left(\sum_{i=0}^{N-1}\lambda^{i}\mathbf{f}^{N-1-i}\right) \\
&= \left(\frac{1}{\alpha}\right)^{N}\mathrm{var}\left(\mathbf{Y}^{0}\right) + \left(\sum_{i=0}^{N-1}\left(\frac{1}{\alpha}\right)^{i}\sigma^{2}\right) + \left(\frac{\Delta t}{\Delta T}\right)^{2}\mathrm{var}\left(\sum_{i=0}^{N-1}\lambda^{i}\mathbf{f}^{N-1-i}\right) \\
&= \left(\frac{1}{\alpha}\right)^{N}\mathrm{var}\left(\mathbf{Y}^{0}\right) + \sigma^{2}\sum_{i=0}^{N-1}\left(\frac{1}{\alpha}\right)^{i} + \left(\frac{\Delta t}{\Delta T}\right)^{2}\mathrm{var}\left(\sum_{i=0}^{N-1}\lambda^{i}\mathbf{f}^{N-1-i}\right)
\end{aligned} \tag{79}$$

Assuming that $1 \,/\, \alpha^{N} \to 0$, Equation 79 becomes

$$\mathrm{var}\left(\mathbf{Y}^{N}\right) \approx \sigma^{2}\sum_{i=0}^{N-1}\left(\frac{1}{\alpha}\right)^{i} + \left(\frac{\Delta t}{\Delta T}\right)^{2}\mathrm{var}\left(\sum_{i=0}^{N-1}\lambda^{i}\mathbf{f}^{N-1-i}\right) \tag{80}$$

If the forcing term, i.e., the last term on Equation 80, *is correlated* with itself, then we use a property of the variance that states:

$$\begin{aligned}
\mathrm{var}\left(\sum_{i=1}^{N}c_i\mathbf{X}_i\right) &= \sum_{i,j=1}^{N}c_i c_j\,\mathrm{cov}\left(\mathbf{X}_i,\mathbf{X}_j\right) \\
&= \sum_{i=1}^{N}c_i^{2}\,\mathrm{var}\left(\mathbf{X}_i\right) + \sum_{i\neq j}c_i c_j\,\mathrm{cov}\left(\mathbf{X}_i,\mathbf{X}_j\right)
\end{aligned} \tag{81}$$

where $\mathbf{X}_i$ is a dummy variable, which represents the forcing function at a given time step. We approximate Equation 81 as

$$\begin{aligned}\operatorname{var}\left(\sum_{i=1}^{N} c_i \mathbf{X}_i\right) &= \sum_{i=1}^{N} c_i^2 \operatorname{var}\left(\mathbf{X}_i\right) + \frac{\sum_{i\neq j} c_i c_j \operatorname{cov}\left(\mathbf{X}_i, \mathbf{X}_j\right)}{\sum_{i=1}^{N} c_i^2 \operatorname{var}\left(\mathbf{X}_i\right)} \sum_{i=1}^{N} c_i^2 \operatorname{var}\left(\mathbf{X}_i\right) \\ &= \sum_{i=1}^{N} c_i^2 \operatorname{var}\left(\mathbf{X}_i\right) + \Gamma \sum_{i=1}^{N} c_i^2 \operatorname{var}\left(\mathbf{X}_i\right) \\ &= \left(1+\Gamma\right) \sum_{i=1}^{N} c_i^2 \operatorname{var}\left(\mathbf{X}_i\right) \\ &\approx \left(1+\Gamma\right) \sum_{i=1}^{N} c_i^2 \sigma_{\mathbf{X}}^2 \\ &\approx \left(1+\Gamma\right) \sigma_{\mathbf{X}}^2 \sum_{i=1}^{N} c_i^2 \\ &\approx F \sigma_X^2 \sum_{i=1}^{N} c_i^2 \end{aligned} \tag{82}$$

where $F = 1 + \Gamma$ and the variance of the forcing function, which is generally a function of time, is approximated as a constant, $\operatorname{var}(\mathbf{X}_i) \approx \sigma_X^2$ for all time steps i and

$$\Gamma = \frac{\sum_{i\neq j} c_i c_j \operatorname{cov}\left(\mathbf{X}_i, \mathbf{X}_j\right)}{\sum_{i=1}^{N} c_i^2 \operatorname{var}\left(\mathbf{X}_i\right)} \tag{83}$$

is the ratio between the sum of the off diagonal elements and the sum of the diagonal elements (i.e., the trace) of the covariance matrix of the forcing function. Given an ensemble forcing function, it is straightforward to compute Γ prior to the simulation and apply this value to compute a heuristic value for the upper bound of the variance of the state $\mathbf{Y}^N$.

Substituting Equation 82 into Equation 80, the variance of the state $\mathbf{Y}^N$ becomes

$$\begin{aligned}\operatorname{var}\left(\mathbf{Y}^N\right) &\approx \sigma^2 \sum_{i=0}^{N-1} \left(\frac{1}{\alpha}\right)^i + \left(\frac{\Delta t}{\Delta T}\right)^2 \operatorname{var}\left(\sum_{i=0}^{N-1} \lambda^i \mathbf{f}^{N-1-i}\right) \\ &\approx \sigma^2 \sum_{i=0}^{N-1} \left(\frac{1}{\alpha}\right)^i + \left(\frac{\Delta t}{\Delta T}\right)^2 F \sigma_f^2 \left(\sum_{i=0}^{N-1} \left(\lambda^i\right)^2\right) \\ &\approx \sigma^2 \sum_{i=0}^{N-1} \left(\frac{1}{\alpha}\right)^i + \left(\frac{\Delta t}{\Delta T}\right)^2 F \sigma_f^2 \left(\sum_{i=0}^{N-1} \left(\lambda^2\right)^i\right) \\ &\approx \sigma^2 \sum_{i=0}^{N-1} \left(\frac{1}{\alpha}\right)^i + \left(\frac{\Delta t}{\Delta T}\right)^2 F \sigma_f^2 \sum_{i=0}^{N-1} \left(\frac{1}{\alpha}\right)^i \\ &\approx \left[\sigma^2 + \left(\frac{\Delta t}{\Delta T}\right)^2 F \sigma_f^2\right] \sum_{i=0}^{N-1} \left(\frac{1}{\alpha}\right)^i \end{aligned}$$

and applying a convergent series solution gives

$$\operatorname{var}\left(\mathbf{Y}^N\right) \approx \underbrace{\frac{\alpha}{\alpha - 1}}_{\substack{\text{coefficient} \\ \text{associated} \\ \text{w/damping}}} \left[\underbrace{\sigma^2}_{\text{additive noise}} + \underbrace{\left(\frac{\Delta t}{\Delta T}\right)^2 F \sigma_f^2}_{\substack{\text{intrinsic variability} \\ \text{due to ensemble} \\ \text{forcing conditions}}}\right] = \sigma_{F,\max}^2 \tag{84}$$

The first term within the brackets in Equation 84 represents the variance contribution from the prescribed, 'additive noise' to the model and the second term comes from the 'intrinsic variability' associated with the (self-correlated) ensemble forcing conditions. Without the presence of the damping term, then Equation 84 becomes

$$\mathrm{var}\left(\mathbf{Y}^N\right) \approx N\left[\sigma^2 + \left(\frac{\Delta t}{\Delta T_f}\right)^2 F\sigma_f^2\right] = \left[\sigma^2 + \left(\frac{\Delta t}{\Delta T_f}\right)^2 F\sigma_f^2\right]\frac{t}{\Delta t} \tag{85}$$

as in the case of Equation 72, but here Equation 85 includes the auto-correlation factor F. Notice, that the factor F accounts for the additional variance created from the covariance of the forcing function in time. In this example, the forcing function, Equation 76, which is exclusively driven by the wave height, will be highly correlated with itself, since wave heights generated from propagating storm events evolve over time scales of days.

Figure 11 illustrates an ensemble simulation of the idealized shoreline change model governed by Equation 73. Recall that this simulation is considered to be 'idealized', because the damping term is linearized as in Equation 74, and thus it differs from the ('full') simulations in Figures 3 and 4. In order to maintain consistency with the simulations presented in Results, the model in Figure 11 uses $N_{\mathrm{ens}} = 1{,}000$, $\sigma = 0.2$ m, $\Delta t = 1/8$ days, $\hat{H}_s = 0.8$ m (which is the mean wave height of the wave ensemble at Tairua beach used in Figure 4), $\Delta Y = 10$ m, and $\Delta T = 28$ days. Unlike in Figure 4, the ensemble of wave forcing conditions used in the current simulation is not shown on Figure 11 in order to maintain visual consistency with Figures 6–10. In this case, the wave forcing conditions come from the same ensemble wave forcing conditions at Tairua beach used in Figure 4, for which $F \approx 15$. The top panel of Figure 11 demonstrates that the spread of the ensemble $\mathbf{Y}^n$ grows almost instantaneously but becomes relatively consistent throughout the simulation. The top panel of Figure 11 depicts the equilibrium range given by $\pm 3\sigma_{F,\max}$, based on Equation 84. However, the behavior of this model, unlike the previous idealized models, is clearly non-Gaussian due to the wave forcing ensemble. Hence, the Gaussian-based limits of $\pm 3\sigma_{F,\max}$ (even though they are still presented on Figure 11 for reference) are not as physically meaningful as in the previous examples. Like previously, each ensemble member in the top panel of Figure 11 is colored similarly to the previous simulations in Appendix A, where the colors of individual simulations are based on their sorted position at the end of the simulation. The color gradation in Figure 11 does not appear until very late in the simulation because the wave ensemble with the largest waves at the end of the simulation will dominate the final rank of the beach state across the ensemble. The bottom panel of Figure 11 shows the simulated ensemble variance, $\mathrm{var}\left(\mathbf{Y}^n\right)$, computed from the trajectories of Y shown in the top panel, compared to the theoretical variance growth rate in Equation 85 and the theoretical maximum variance in Equation 84. Overall, the simulated ensemble variance growth rates and limits agree with the theoretical results, with large, temporary deviations from the theoretical constant due to the time-variability of the forcing (which is not accounted for in the theoretical result). Note that here the model variance exhibits some large spikes in model variance associated with large erosion events (shown on the top panel of Figure 11) caused by large wave-height events in certain members of the forcing ensemble. Overall, the agreement of the computed and theoretical variance is excellent in the case presented in Figure 11 and analogously in Figure 4. This validates the relevance of Equation 85 for predicting the uncertainty across the wave forcing ensemble as further explored in the Discussion section.

Example #5: Idealized shoreline change ensemble based on ShoreFor

Finally, we present a brief analysis of an idealized ensemble shoreline change model based on ShoreFor (Davidson et al. 2013). The purpose of this example is to demonstrate that ShoreFor represents a purely forced model (without damping) where the right-hand side of the governing equation is only a function of the wave forcing conditions, like in Equation 11 in Methods. Based on the complete description of ShoreFor in Equation 9, we construct an idealized ShoreFor model as

$$\frac{dY}{dt} = \frac{Y^{n+1} - Y^n}{\Delta t} = f^n\left(\Omega_{\mathrm{eq}}^{n-1} - \Omega^n\right) \tag{86}$$

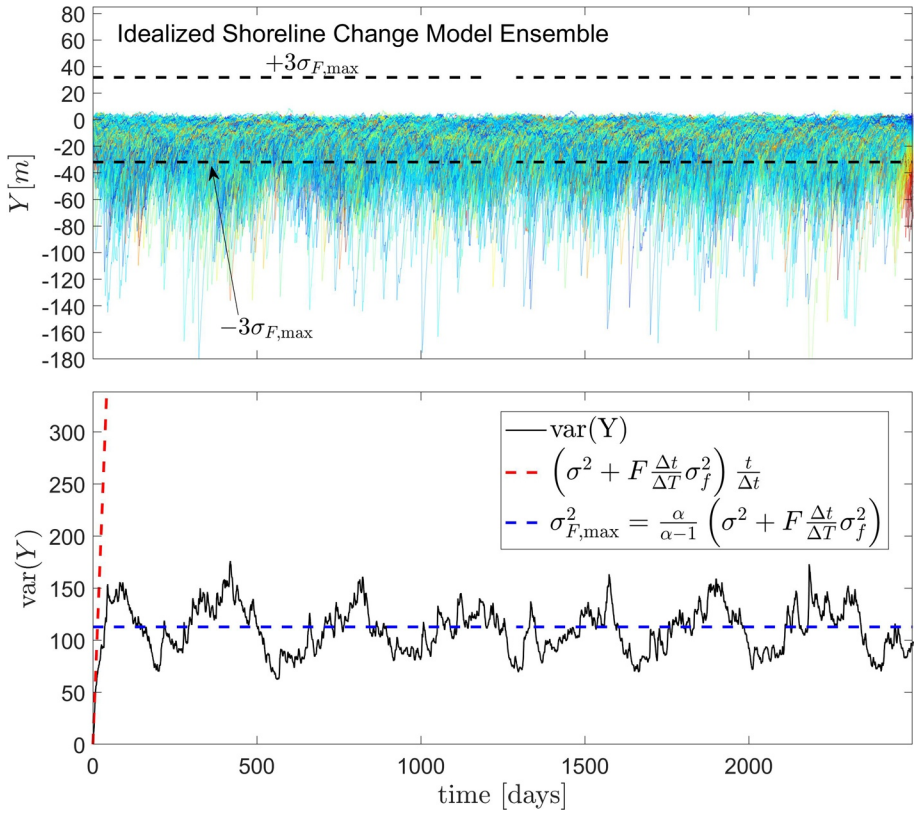

Figure 11. An ensemble simulation of an idealized shoreline change model governed by Equation 73 with $N_{\mathrm{ens}} = 1{,}000$, $\sigma = 0.2$ m, $\Delta t = 1/8$ days, $\hat{H}_s = 0.8$ m, $\Delta Y = 10$ m, and $\Delta T = 28$ days. The forcing f, in this example (not shown), is the same the ensemble wave forcing used in the simulations shown in Figure 4. The top panel shows that the model trajectories of each member of the ensemble, which are colored similarly to the previous figures, are not well bounded by $\pm 3\sigma_{F,\max}$, because unlike the previous examples, the behavior of the beach state is non-Gaussian owing to the wave forcing. The bottom panel shows the simulated ensemble variance, computed from the trajectories of Y shown in the top panel, compared to the theoretical variance growth rate given in Equation 85 in the absence of damping, and the theoretical upper limit to the variance, $\sigma^2_{F,\max}$, based on Equation 84. Note that here the model variance exhibits some large fluctuations, the peaks of which are generally associated with large erosion events (shown on the top panel) caused by large wave-height events in certain members of the forcing ensemble.

where f^n represents the wave forcing function (e.g., wave power in Equation 9), which includes the relevant modifying coefficients, and $\Omega_{\mathrm{eq}}^{n-1} - \Omega^n$ represents the disequilibrium state. We apply an idealized memory decay function for $\Omega_{\mathrm{eq}}^{n-1}$, which represents a simplification of the complete function in Equation 10. We construct an idealized memory decay function as

$$\Omega_{\mathrm{eq}}^{n-1} = 0.1\Omega^{n-1} + 0.01\Omega^{n-2}. \tag{87}$$

The memory decay function in Equation 87 only involves the previous two values of Ω. However, we investigate a general memory decay function (of arbitrary length) later in this section.

Combining Equations 86 and 87, we derive the update equation for the shoreline position as

$$\frac{dY}{dt} = \frac{Y^{n+1} - Y^n}{\Delta t} = f^n\left(-\Omega^n + 0.1\Omega^{n-1} + 0.01\Omega^{n-2}\right)$$

$$Y^{n+1} = Y^n + \Delta t f^n\left(-\Omega^n + 0.1\Omega^{n-1} + 0.01\Omega^{n-2}\right) \tag{88}$$

Evaluating Equation 88 over the first few time steps gives

$$Y^n = Y^0 - \Delta t \sum_{i=0}^{n-1} f^i \Omega^i + 0.1\Delta t \sum_{i=0}^{n-2} f^{i+1} \Omega^i + 0.01\Delta t \sum_{i=0}^{n-3} f^{i+2} \Omega^i \tag{89}$$

We generalize the result found in Equation 89, by using a generalized, 3-term memory decay function of the form

$$\Omega_{\text{eq}}^{n-1} = c_1 \Omega^{n-1} + c_2 \Omega^{n-2} + c_3 \Omega^{n-3}. \tag{90}$$

Combining the idealized ShoreFor governing equation in Equation 86 with the memory decay function in Equation 90 results in

$$Y^n = Y^0 - \Delta t \sum_{i=0}^{n-1} f^i \Omega^i + c_1 \Delta t \sum_{i=0}^{n-2} f^{i+1} \Omega^i + c_2 \Delta t \sum_{i=0}^{n-3} f^{i+2} \Omega^i + c_3 \Delta t \sum_{i=0}^{n-4} f^{i+3} \Omega^i. \tag{91}$$

Further still, we generalize the result found in Equation 91, by applying a N_c-term memory decay function of the form

$$\Omega_{eq}^{n-1} = c_1 \Omega^{n-1} + c_2 \Omega^{n-2} + c_3 \Omega^{n-3} + \ldots + c_{N_c-1} \Omega^{n-N_c-1} + c_{N_c} \Omega^{n-N_c}. \tag{92}$$

Combining the idealized ShoreFor governing equation in Equation 86 with the generalized, N_c-term memory decay function in Equation 92 gives

$$Y^n = Y^0 + \Delta t \underbrace{\sum_{k=0}^{N_c} \left(c_k \sum_{i=0}^{n-1-k} f^{i+k} \Omega^i \right)}_{\text{generalized wave forcing conditions}} = Y^0 + \Delta t \, \tilde{f}^n \left(f^1, f^2, \cdots, f^{n-1}, \Omega^1, \Omega^2, \cdots, \Omega^n, c_0, c_1, \cdots, c_{N_c} \right) \tag{93}$$

where $c_0 = -1$ and c_1 through c_{N_c} can be generated from an arbitrary decaying function, for example $c_1 = 0.1, c_2 = 0.01, c_3 = 0.001$, etc.

Notice that Equation 93 is purely determined by the generalized, time-varying forcing function, $\tilde{f}^n$, which represents a combination of the antecedent wave conditions (f and Ω) and the model parameters (c).

Thus, the ShoreFor model, as demonstrated in Equation 93, can be written entirely in terms of a forced, ordinary differential equation of the form

$$\frac{dY}{dt} = \underbrace{f(t)}_{\text{wave forcing}} \tag{94}$$

as in Equation 11 in Methods.

Here, we *do not* seek to quantify the uncertainty of the idealized model presented in Equation 93, because the uncertainty is purely a function of the forcing term which can vary greatly from model to model. Additionally, because Equations 93 and 94 lack any explicit form of shoreline-state-dependent damping, the uncertainty of this model will not be bounded as in the previous examples (#'s 2–4). Due to the lack of damping, the "beach memory" of Equation 93 is perfect. The initial condition in Equation 93, Y^0, is never 'forgotten' as it is in Equations 53, 63, and 77. Thus, the preceding analysis demonstrates that ensemble variance of the idealized ShoreFor model (Equation 93) is allowed to grow without constraint at the direction of the specific forcing functions applied to it. Comparing ShoreFor, e.g., Equation 93, with Yates et al. (2009), e.g., Equation 77, we see that fundamental and "philosophical" differences exist between these two most popular equilibrium shoreline models.

Data Availability Statement

All wave, shoreline data, and code used here are available at https://coastalhub.science/data.

Acknowledgments
The authors thank Phillipe Wernette for conducting a U.S. Geological Survey (USGS) internal review of this manuscript. The authors thank the three anonymous journal reviewers and the editors for their comments and suggestions, which lead to a significant improvement of this manuscript. This work was funded by the USGS Coastal and Marine Hazards and Resources Program under co-op agreement G16AC00275. Development of the ensemble Kalman filter version of CoSMoS-COAST (Vitousek et al., 2017) was conducted while Sean Vitousek was at the University of Illinois at Chicago preparing for the invited "Shoreshop" workshop (Montaño et al., 2020) and coastal change prediction competition in Auckland, NZ in summer 2018. Funding for Shoreshop from the Auckland Hazard Hub awarded to Giovanni Coco (Climate change impacts on weather related hazards) is gratefully acknowledged. The idea to develop an ensemble coastal change prediction model based on multiple realizations of a stochastic wave climate grew out of the Shoreshop workshop and subsequent discussions. The analysis of the model uncertainty and the writing of the manuscript were conducted while Sean Vitousek was at the USGS in Santa Cruz, CA. Any use of trade, firm, or product names is for descriptive purposes onlyand does not imply endorsement by the U.S. Government.

References

Anderson, D., Rueda, A., Cagigal, L., Antolinez, J. A. A., Mendez, F. J., & Ruggiero, P. (2019). Time-varying emulator for short and long-term analysis of coastal flood hazard potential. *Journal of Geophysical Research: Oceans*, *124*(12). 9209–9234. https://doi.org/10.1029/2019JC015312

Antolínez, J. A. A., Méndez, F. J., Anderson, D., Ruggiero, P., Kaminsky, & George, M. (2019). Predicting climate driven coastlines with a simple and efficient multi-scale model. *Journal of Geophysical Research: Earth Surface*, *124*(6), 1596–1624. https://doi.org/10.1029/2018JF004790

Antolínez, J. A. A., Méndez, F. J., Camus, P., Vitousek, S., Mauricio González, E., Ruggiero, P., & Barnard, P. (2016). A multiscale climate emulator for long-term morphodynamics (MUSCLE-morpho). *Journal of Geophysical Research: Oceans*, *121*(1), 775–791. https://doi.org/10.1002/2015JC011107

Bannister, R. N. (2017). A review of operational methods of variational and ensemble-variational data assimilation. *Quarterly Journal of the Royal Meteorological Society*, *143*(703), 607–633.

Banno, M., Kuriyama, Y., & Hashimoto, N. (2015). Equilibrium-based foreshore beach profile change model for long-term data. *The Proceedings of the Coastal Sediments 2015*.

Blossier, B., Bryan, K. R., Daly, C. J., Winter, C. (2017a). Spatial and temporal scales of shoreline morphodynamics derived from video camera observations for the island of Sylt, German Wadden Sea. *Geo-Marine Letters 37*(2), 111–123.

Blossier, B., Bryan, K. R., Daly, C. J., & Winter, C. (2017b). Shore and bar cross-shore migration, rotation, and breathing processes at an embayed beach. *Journal of Geophysical Research: Earth Surface*, *122*(10), 1745–1770.

Cagigal, L., Rueda, A., Anderson, D., Ruggiero, P., Merrifield, M. A., Montaño, J., et al. (2020). A multivariate, stochastic, climate-based wave emulator for shoreline change modeling. *Ocean Modelling*, 101695.

Callaghan, D. P., Roshanka, R., & Dano, R. (2013). Probabilistic estimation of storm erosion using analytical, semi-empirical, and process based storm erosion models. *Coastal Engineering*, *82*, 64–75.

Camus, P., Losada, I. J., Izaguirre, C., Espejo, A., Menéndez, M., Pérez, J., et al. (2017). Statistical wave climate projections for coastal impact assessments. *Earth's Future 5*(9), 918–933.

Castelle, B., Marieu, V., Bujan, S., Ferreira, S., Parisot, J.-P., Capo, S., et al. (2014). Equilibrium shoreline modeling of a high-energy meso-macrotidal multiple-barred beach. *Marine Geology*, *347*, 85–94.

Cowell, P. J., Thom, B. G., Jones, R. A., Everts, C. H., & Simanovic, D. (2006). Management of uncertainty in predicting climate-change impacts on beaches. *Journal of Coastal Research*, *22*(1), 232–245.

D'Anna, M., Idier, D., Castelle, B., Rohmer, J., Le Cozannet, G., & Robinet, A. (2020). Impact of model free parameters and sea-level rise uncertainties on 20-years shoreline hindcast: The case of Truc Vert beach (SW France). *Earth Surface Processes and Landforms*, *45*(8), 1895–1907.

Davidson, M. A., Lewis, R. P., & Turner, I. L. (2010). Forecasting seasonal to multi-year shoreline change. *Coastal Engineering*, *57*(6), 620–629.

Davidson, M. A., Splinter, K. D., & Turner, I. L. (2013). A simple equilibrium model for predicting shoreline change. *Coastal Engineering*, *73*, 191–202.

Davidson, M. A., Turner, I. L., Splinter, K. D., & Harley, M. D. (2017). Annual prediction of shoreline erosion and subsequent recovery. *Coastal Engineering*, *130*, 14–25.

Ding, Y., Frey, A. E., Kim, S.-C., & Permenter, R. E. (2018). Probabilistic shoreline change modeling and risk estimation of erosion. *Coastal Engineering Proceedings*, *1*(36), 1.

Evensen, G. (1994). Sequential data assimilation with a nonlinear quasi-geostrophic model using Monte Carlo methods to forecast error statistics. *Journal of Geophysical Research*, *99*(C5), 10143–10162.

Evensen, G. (2003). The ensemble Kalman filter: Theoretical formulation and practical implementation. *Ocean Dynamics*, *53*(4), 343–367.

Hegermiller, C. A., Erikson, Li H., & Barnard, P. L. (2016). Nearshore waves in Southern California: Hindcast, and modeled historical and 21stcentury projected time series. *US Geological Survey summary of methods to accompany data release*. 1–118.

Jara, M. S., González, M., & Medina, R. (2015). Beach memory related to cross-shore processes. *The Proceedings of the Coastal Sediments 2015*.

Jara, M. S., González, M., Medina, R., & Jaramillo, C. (2018). Time-Varying Beach Memory Applied to Cross-Shore Shoreline Evolution Modeling. *Journal of Coastal Research*, *34*(5), 1256–1269.

Jones, P. W., & Smith, P. (2017). *Stochastic processes: An introduction*. CRC Press.

Kroon, A., de Schipper, M., Pieter van Gelder, & Aarninkhof, S. (2020). Ranking uncertainty: Wave climate variability versus model uncertainty in probabilistic assessment of coastline change. *Coastal Engineering*, *103673*.

Le Cozannet, G., Bulteau, T., Castelle, B., Ranasinghe, R., Wöppelmann, G., Rohmer, J., et al. (2019). Quantifying uncertainties of sandy shoreline change projections as sea level rises. *Scientific Reports*, *9*(1), 1–11.

Lemos, C., Floc'h, F., Yates, M., Le Dantec, N., Marieu, V., Hamon, K. & Delacourt, C. (2018). Equilibrium modeling of the beach profile on a macrotidal embayed low tide terrace beach. *Ocean Dynamics*, *68*(9), 1207–1220.

Limber, P. W., Barnard, P. L., Vitousek, S., & Erikson, Li H. (2018). A model ensemble for projecting multidecadal coastal cliff retreat during the 21st century. *Journal of Geophysical Research: Earth Surface*, *123*(7), 1566–1589.

Long, J. W., & Plant, N. G. (2012). Extended Kalman Filter framework for forecasting shoreline evolution. *Geophysical Research Letters*, *39*, 13.

Masselink, G., Castelle, B., Scott, T., Dodet, G., Suanez, S., Jackson, D., & Floc'h, F. (2016). Extreme wave activity during 2013/2014 winter and morphological impacts along the Atlantic coast of Europe. *Geophysical Research Letters*, *43*(5), 2135–2143.

Miller, J. K., & Dean, R. G. (2004). A simple new shoreline change model. *Coastal Engineering*, *51*, 7–556–531.

Moin, P. (2010). *Fundamentals of engineering numerical analysis*, Cambridge University Press.

Montaño, J., Coco, G., Antolinez, J. A. A., Beuzen, T., Bryan, K. R., Cagigal, L., et al. (2020). Blind testing of shoreline evolution models. *Scientific Reports*, *10*(1), 1–10.

Morim, J., Hemer, M., Wang, X. L., Cartwright, N., Trenham, C., Semedo, A., et al. (2019). Robustness and uncertainties in global multivariate wind-wave climate projections. *Nature Climate Change*, *9*(9), 711–718.

Murray, A. B., Gasparini, N. M., Goldstein, E. B., & van der Wegen, M. (2016). Uncertainty quantification in modeling earth surface processes: more applicable for some types of models than for others. *Computers & Geosciences*, *90*, 6–16.

Papoulis, A., & Pillai, S. U. (2002). *Probability, random variables, and stochastic processes*. Tata McGraw-Hill Education.

Pelnard-Considère, R. (1957). Essai de theorie de l'evolution des formes de rivage en plages de sable et de galets. *Journées de l'hydraulique*, *4*(1), 289–298.

Pérez, J., Méndez, F. J., Menéndez, M., & Losada, I. J. (2014). ESTELA: A method for evaluating the source and travel time of the wave energy reaching a local area. *Ocean Dynamics 64*(8) 1181–1191.

Ranasinghe, R. (2020). On the need for a new generation of coastal change models for the 21st century. *Scientific Reports*, *10*(1). 1–6.

Ranasinghe, R., Callaghan, D., & Stive, M. J. F. (2012). Estimating coastal recession due to sea level rise: Beyond the Bruun rule. *Climatic Change*, *110*, 561–574 4-Mar.

Reeve, D. E., & Fleming, C. A. (1997). A statistical-dynamical method for predicting long term coastal evolution. *Coastal Engineering*, *30*, 259–280 4-Mar.

Reeve, D. E., Karunarathna, H., Pan, S., Horrillo-Caraballo, Jose, M., Różyński, G., & Ranasinghe, R. (2016). Data-driven and hybrid coastal morphological prediction methods for mesoscale forecasting. *Geomorphology*, *256*, 49–67.

Reeve, D. E., Pedrozo-Acuña, A., & Spivack, M. (2014). Beach memory and ensemble prediction of shoreline evolution near a groyne. *Coastal Engineering*, *86*, 77–87.

Robinet, A., Castelle, B., Idier, D., Le Cozannet, G., Déqué, M., & Charles, E. (2016). Statistical modeling of interannual shoreline change driven by North Atlantic climate variability spanning 2000–2014 in the Bay of Biscay. *Geo-Marine Letters*, *36*(6), 479–490.

Robinet, A., Idier, D., Castelle, B., & Marieu, V. (2018). A reduced-complexity shoreline change model combining longshore and cross-shore processes: the LX-Shore model. *Environmental Modelling & Software*, *109*, 1–16.

Roelvink, D. (2011). *A guide to modeling coastal morphology 12*.

Roelvink, J. A., & Walstra, D.-J. (2004). Keeping it simple by using complex models. *Advances in Hydro-science and Engineering*, *6*, 11.

Roy, C. J., & Oberkampf, W. L. (2011). A comprehensive framework for verification, validation, and uncertainty quantification in scientific computing. *Computer Methods in Applied Mechanics and Engineering*, *200*(25–28), 2131–2144.

Rueda, A., Hegermiller, C. A., Antolinez, J. A. A., Camus, P., Vitousek, S., Ruggiero, P., et al. (2017). Multiscale climate emulator of multi-modal wave spectra: MUSCLE-spectra. *Journal of Geophysical Research: Oceans*, *122*(2), 1400–1415.

Ruggiero, P., List, J., Hanes, D., & Eshleman, J. (2006). Probabilistic shoreline change modeling. *Coastal Engineering*. *5*, 3417–3429.

Splinter, K. D., Turner, I. L., Davidson, M. A., Barnard, P., Castelle, B., & Oltman-Shay, J. (2014). A generalized equilibrium model for predicting daily to interannual shoreline response. *Journal of Geophysical Research: Earth Surface*, *119*(9), 1936–1958.

Turki, I., Medina, R., Coco, G., & Gonzalez, M. (2013). An equilibrium model to predict shoreline rotation of pocket beaches. *Marine Geology*, *346*, 220–232.

Turki, I., Medina, R., & Gonzalez, M. (2012). Beach Memory. *Coastal Engineering Proceedings*, *1*(33),.49

Van de Lageweg, W. I., Bryan, K. R., Coco, G., & Ruessink, B. G. (2013). Observations of shoreline–sandbar coupling on an embayed beach. *Marine Geology*, *344*, 101–114.

Vitousek, S., & Barnard, P. L. (2015). *The Proceedings of the Coastal Sediments*.A nonlinear, implicit one-line model to predict long-term shoreline change

Vitousek, S., Barnard, P. L., & Limber, P. (2017). Can beaches survive climate change? *Journal of Geophysical Research: Earth Surface*, *122*(4), 1060–1067.

Vitousek, S., Barnard, P. L., Limber, P., Erikson, L., & Cole, B. (2017). A model integrating longshore and cross-shore processes for predicting long-term shoreline response to climate change. *Journal of Geophysical Research: Earth Surface*, *122*(4), 782–806. https://doi.org/10.1002/2016JF004065

Vrijling, J. K., & Meijer, G. J. (1992). Probabilistic coastline position computations. *Coastal Engineering*, *17*(1–2), 1–12.

Walker, W. E., Harremoës, P., Rotmans, J., Van Der Sluijs, J. P., Van Asselt, M. B., Janssen, P., & Krayer von Krauss, M. P. (2003).Defining uncertainty: a conceptual basis for uncertainty management in model-based decision support. *Integrated Assessment*, *4*(1).

Wang, B., & Reeve, D. (2010). Probabilistic modeling of long-term beach evolution near segmented shore-parallel breakwaters. *Coastal Engineering*, *57*(8), 732–744.

Wilson, G. W., Özkan-Haller, H. T., & Holman, R. A. (2010). Data assimilation and bathymetric inversion in a two-dimensional horizontal surf zone model. *Journal of Geophysical Research: Oceans*, *115*(C12).

Wilson, G. W., Özkan-Haller, H. T., Holman, R. A., Haller, M. C., Honegger, D. A., & Chickadel, C. C. (2014). Surf zone bathymetry and circulation predictions via data assimilation of remote sensing observations. *Journal of Geophysical Research: Oceans*, *119*(3), 1993–2016.

Wright, L. D., & Short, A. D. (1984). Morphodynamic variability of surf zones and beaches: a synthesis. *Marine Geology*, *56*, 93–118.

Wright, L. D., Short, A. D., & Green, M. O. (1985). Short-term changes in the morphodynamic states of beaches and surf zones: An empirical predictive model. *Marine Geology*, *62*, 339–364.

Yates, M. L., Guza, R. T., & O'reilly, W. C. (2009). Equilibrium shoreline response: Observations and modeling. *Journal of Geophysical Research: Oceans*, *114*, C9.

Zacharioudaki, A., & Reeve, D. E. (2011). Shoreline evolution under climate change wave scenarios. *Climatic Change*, *108*,73–105.